

The Cogne magnetite deposit (Western Alps, Italy): A Late Jurassic seafloor ultramafic-hosted hydrothermal system?



Luca Toffolo^{a,*}, Paolo Nimis^a, Silvana Martin^a, Simone Tumiati^b, Wolfgang Bach^c

^a Geosciences Department, University of Padua, via Gradenigo 6, 35100 Padua, Italy

^b Earth Sciences Department, University of Milan, via Mangiagalli 34, 20133 Milan, Italy

^c Department of Geosciences and MARUM Center for Marine Environmental Sciences, P.O. Box 330440, 28334 Bremen, Germany

ARTICLE INFO

Article history:

Received 26 July 2016

Received in revised form 23 November 2016

Accepted 24 November 2016

Available online 1 December 2016

ABSTRACT

The Cogne magnetite deposit (Western Alps, Italy) is the largest in a series of apatite and sulphide-free magnetite orebodies that are hosted in serpentinites belonging to western Alpine ophiolitic units. The nearly endmember composition of magnetite, which is unusual for an ultramafic setting, and the relatively high tonnage of the deposit ($18 \cdot 10^6$ tonnes at 45–50 wt% Fe) make Cogne an intriguing case study to explore magnetite-forming processes in ophiolites. The Cogne magnetite shows variable textures, including nodular ores, veins and fine-grained disseminations in serpentinites after mantle peridotites and totally serpentinitized melt-impregnated peridotites (troctolites). An increase in Co/Ni ratio from magnetite-poor serpentinitized peridotites (0.05) to nodular magnetite ores (>1) is observed. Trace element analyses of magnetite from different sites and lithologies by laser-ablation inductively-coupled mass spectrometry indicate that magnetites have typical hydrothermal compositions, characterized by high Mg and Mn (median values up to ~24,100 and ~5000 ppm, respectively), and low Cr, Ti and V (median values up to ~30, ~570 and ~60 ppm, respectively). Moreover, the variations in trace element compositions distinguish magnetite that is hydrothermal fluid-controlled [highest (Mg, Mn, Co, Zn)/Ni ratios] from magnetite whose composition is affected by host-rock chemistry (highest Ni \pm Ti \pm V). U-Th-Pb dating of magnetite-associated uraninite constrains the formation of the deposit to the Late Jurassic (ca. 150 Ma), during an advanced stage of the opening of the Alpine Tethys. Thermodynamic modelling of fluid-rock interactions indicates that fluids produced by seawater-peridotite or seawater-Fe-gabbro are not sufficiently Fe-rich to account for the formation of the Cogne deposit. This suggests that fractionation processes such as phase separation were critical to generate hydrothermal fluids capable to precipitate large amounts of magnetite in various types of ultramafic host-rocks. The oceanic setting and geochemical and mineralogical similarities with some modern ultramafic-hosted volcanogenic massive sulphide deposits on mid-ocean ridges suggest that the exposed mineralized section at Cogne may represent the deep segment of a seafloor, high-temperature (~300–400 °C) hydrothermal system. The occurrence of similar magnetite enrichments in present-day oceanic settings could contribute to explain the presence of significant magnetic anomalies centred on active and inactive ultramafic-hosted hydrothermal fields.

© 2016 Elsevier B.V. All rights reserved.

1. Introduction

The Cogne mining district (southern Valle d'Aosta region, Western Alps, Italy; Fig. 1) consists of a set of mines, which exploited a magnetite-rich serpentinite unit from the Middle Ages to 1979. The tonnage of the ore deposit was estimated at 18 Mt (Nazionale "Cogne" S.p.a., 1954), and the run-of-mine ore produced in the

1960s had an iron grade of 45–50% (Di Colbertaldo et al., 1967). The Cogne deposit is the largest in a series of apatite and sulphide-free serpentinite-hosted magnetite orebodies that crop out in ophiolitic units along the western Alpine collisional suture in Valle d'Aosta (Castello, 1981; Diella et al., 1994; Rossetti et al., 2009; Stella, 1921) and in its southern extension in Corsica (Fari-nole mine; Routhier, 1963). In southern Valle d'Aosta, most of these magnetite orebodies occur in the Mt. Avic serpentinite massif (located ca. 15 km ENE of the Cogne serpentinite; Fig. 1) and have been interpreted as former metasomatized podiform chromitites, based on their high Cr concentration and the presence of chromite relicts (Diella et al., 1994; Della Giusta et al., 2011; Rossetti et al.,

* Corresponding author.

E-mail addresses: luca.toffolo@phd.unipd.it (L. Toffolo), paolo.nimis@unipd.it (P. Nimis), silvana.martin@unipd.it (S. Martin), simone.tumiati@unimi.it (S. Tumiati), wbach@uni-bremen.de (W. Bach).

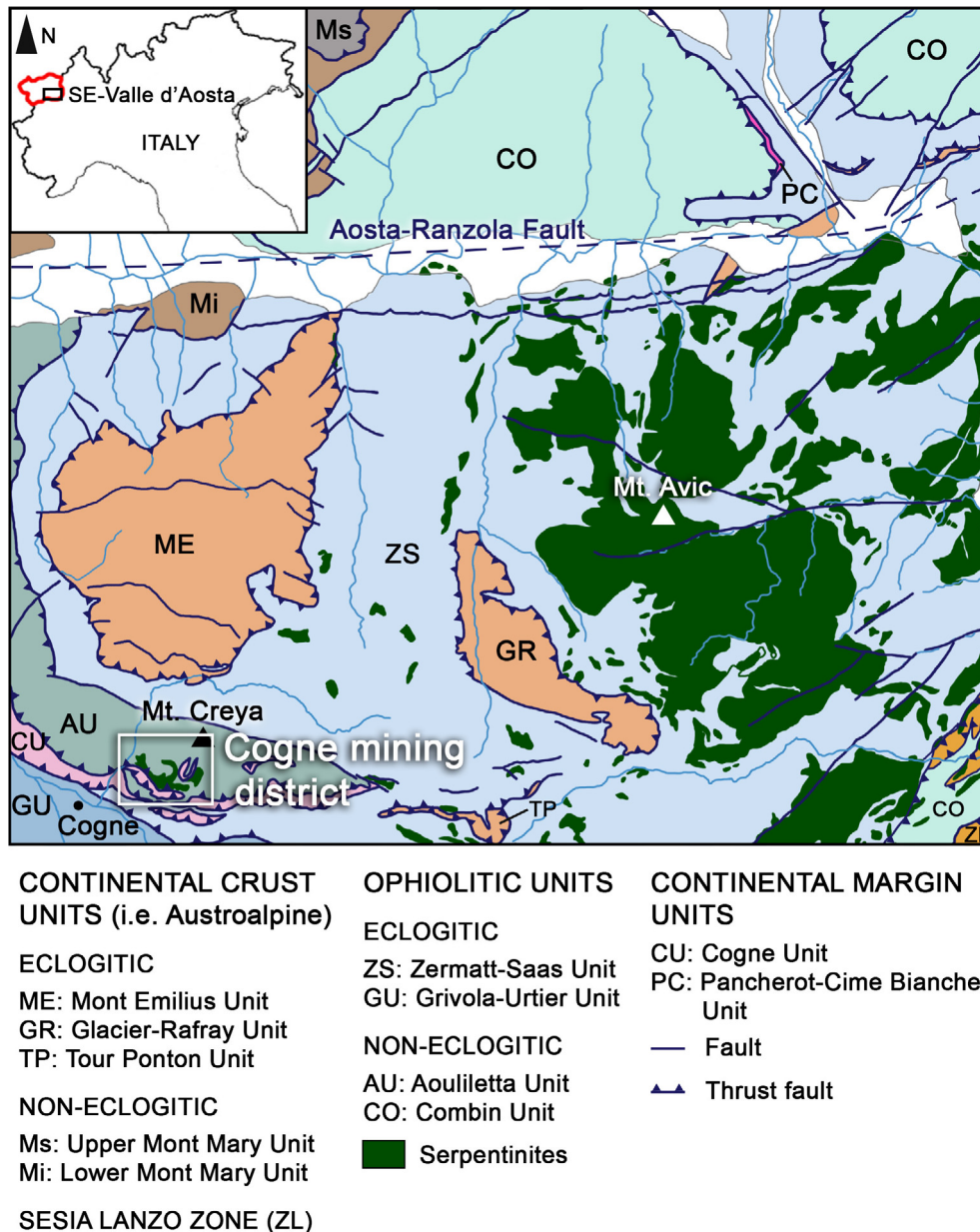


Fig. 1. Geological map of the southern Valle d'Aosta region. Redrawn and modified after De Giusti et al. (2003) and Dal Piaz et al. (2010).

2009). A similar origin has been proposed for analogous Mesozoic (probably Jurassic), ophiolite-hosted magnetite deposits in Greece (Vermion, Olympus and Edessa regions and Skyros island; Paraskevopoulos and Economou, 1980). The Cogne deposit differs from the above occurrences because its magnetite has a nearly pure endmember composition and contains only trace amounts of compatible elements such as Cr, Ti and V (Carbonin et al., 2014; Compagnoni et al., 1981). This geochemical fingerprint, which is unusual for an ultramafic setting, as well as the relatively high tonnage of the deposit, make Cogne an interesting and still poorly studied example of ophiolite-hosted magnetite deposit. Understanding its genesis may have implications for our interpretation of magnetic anomalies reported from modern ultramafic-hosted hydrothermal sites on slow-spreading mid-ocean ridges (Fujii et al., 2016; Sztikar et al., 2014; Tivey and Dymont, 2010).

Several hypotheses have been put forward to explain the genesis of the Cogne deposit. Di Colbertaldo et al. (1967) proposed a genesis by magmatic segregation from an ultramafic melt. Based

on the Cr and Ti-poor composition of the magnetite, Compagnoni et al. (1979, 1981) ascribed the formation of the Cogne magnetite to high-temperature serpentinization of oceanic peridotites and consequent Fe mobilization, but they did not discuss this hypothesis in detail. Recently, Carbonin et al. (2014) investigated some of the magnetite-associated lithologies and suggested their possible hydrothermal origin; however, the ore-forming processes were not explored.

In this paper, we present new petrographic and geochemical data on the Cogne deposit, focusing on the textural relationships and the trace element composition of magnetite. The latter has been a valuable tool in the identification of the petrogenetic environment (e.g., Boutroy et al., 2014; Dare et al., 2014; Dupuis and Beaudoin, 2011; Nadoll et al., 2014, 2015). In addition, we determine for the first time the radiometric age of the magnetite orebody by U–Th–Pb dating of uraninite. We will show that the magnetite geochemistry and age support a seafloor oceanic hydrothermal setting for the Cogne deposit, and we will explore

the possible formation mechanisms, using constraints from geochemical modelling of seawater-rock reactions.

2. Geology of the Cogne mining area

The Cogne serpentinite is a 2.5 km long sliver, with an average thickness of 100 m (Di Colbertaldo et al., 1967), which is exposed on the S and W slopes of Montzalet (Figs. 1 and 2). The serpentinite is tectonically sandwiched between two different metasedimentary sequences. The foot wall sequence consists of tectonically juxtaposed slivers of calcschists, marbles, dolomitic marbles and quartzites formed in a continental margin and in other paleogeographic domains (Cogne Unit; Polino et al., 2014). The hanging wall sequence is represented by calcschists, marbles and minor, Fe- and Mn-bearing metacherts. The basal contact of the serpentinite is a thrust fault (Elter, 1971), while the upper limit is marked by a few cm- to 3 m-thick boudinaged rodingite, which we tentatively interpret as a tectonically activated, primary serpentinite-sediment interface. According to Elter (1971), the Cogne serpentinite and the hanging wall metasediments form the core of a km-scale isoclinal fold that repeats the Cogne unit in its upper limb (Fig. 2b). The Cogne serpentinite and the hanging wall metasedi-

ments are considered to be part of the same greenschist- to blueschist-facies ophiolite-bearing unit (Aouilletta Unit; Polino et al., 2014), which is sandwiched together with the foot wall marbles and quartzites between two eclogite-facies ophiolitic units (Grivola-Urtier Unit and Zermatt-Saas Unit; Dal Piaz et al., 2010). These ophiolitic units are remnants of the Jurassic Piedmont-Liguria ocean (Alpine Tethys; Schmid et al., 2004; Stampfli, 2000). From Late Cretaceous to Eocene, these ophiolitic units followed different P-T paths related to their subduction beneath the Adriatic micro-plate, as a result of Africa-Europe convergence (Schmid et al., 2004). In the Zermatt-Saas Unit (in southern Valle d'Aosta), the high-pressure (eclogitic) metamorphic peak was reached in the Eocene (45–42 Ma; Dal Piaz et al., 2001), contemporaneously with the closure of the ocean (Dal Piaz et al., 2003), and was followed by a greenschist-facies overprint during Late Eocene-Early Oligocene (Dal Piaz et al., 2001, 2003). No P-T-time estimate is available for the Cogne serpentinite and its host Aouilletta Unit.

The Cogne magnetite mineralization is confined to the serpentinite body (Compagnoni et al., 1979; Di Colbertaldo et al., 1967) and it is exposed in three zones, henceforward referred to as Site 1, Site 2 and Site 3 (Fig. 2). At Site 1 (which includes the mines of Liconi, 45.612509 N 7.395377 E, Colonna, 45.609716 N

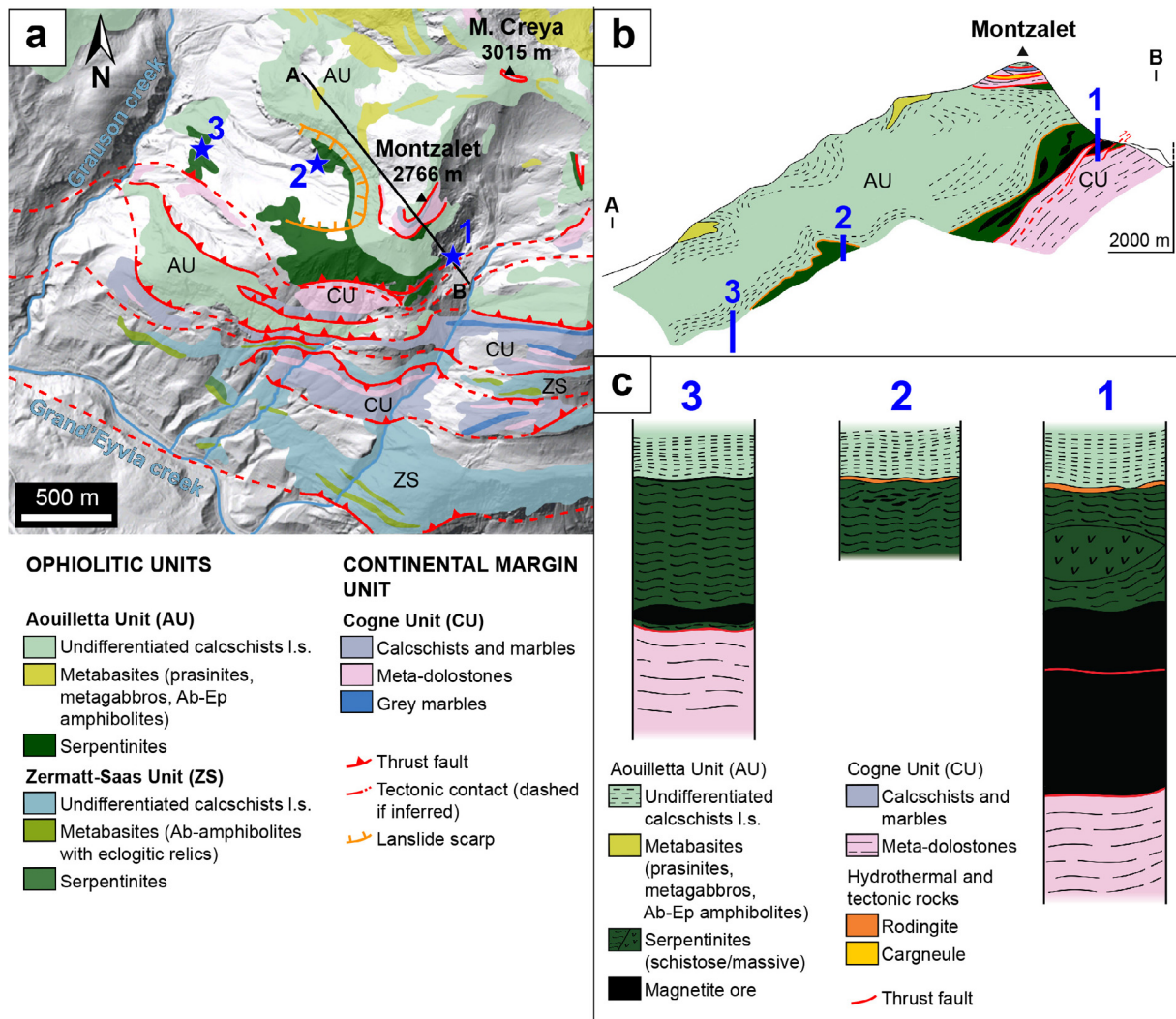


Fig. 2. a) Simplified geologic map of the Cogne mining district showing the structural relationships between the Cogne serpentinite and the associated units. Numbered stars indicate the sampling sites (see text for details). Units after Dal Piaz et al. (2010); digital terrain map (DTM) from “Agenzia Regionale per la Protezione Ambientale” (ARPA) Piemonte. b) Geological profile through the Cogne serpentinite. Redrawn and modified after Elter (1971). c) Pseudostratigraphic columns of the three sampling sites.

7.391322 E, and Costa del Pino, 45.610466 N 7.378247 E), the orebody is a 50–70 m-thick, 600 m-long continuous lens that dips and wedges out northward (Di Colbertaldo et al., 1967). This orebody was extensively exploited in the second half of the twentieth century by sublevel caving. At Site 2 (western slope of Montzalet, 45.618124 N 7.386316 E) and Site 3 (Larsinaz mine, 45.619119 N 7.377135 E), the intensely mineralized rock volumes are much smaller, and consist of disseminations and veins at Site 2 and of a less than 10 m-thick lens at Site 3 (Stella, 1916). The mineralized serpentinite was subjected to only low degrees of Alpine deformation and metamorphism (Carbonin et al., 2014), which allowed extensive preservation of the original structures (see below).

3. Materials and methods

3.1. Petrographic and mineralogical analysis

Sixty-eight rock samples from the Cogne mining area were collected from mine dumps and outcrops and studied by means of optical microscopy in thin polished sections. No potential source of lead was present during any stage of the sample preparation, to avoid contamination that could invalidate the subsequent geochronological analyses. Mineral identification was aided by micro-Raman spectroscopy, using a Thermo Scientific™ DXR™ confocal Raman system at the Chemistry Department of the University of Padua (Italy). We chose a 532 nm laser working at a power of 5–10 mW. All of the Raman spectra were collected with a 50× LWD objective lens, reaching a spatial resolution of ~1 μm. Raman spectroscopy was crucial for the identification of serpentine minerals, for which we followed the guidelines by Groppo et al. (2006) and Carbonin et al. (2014). Selected samples were further investigated using a scanning electron microscope (SEM). Back-scattered electron (BSE) images were obtained using a CamScan MX 2500 SEM at the Department of Geosciences of the University of Padua (Italy) equipped with a LaB₆ crystal, working at 20 kV accelerating voltage and 140 nA current.

Mineral compositions of major minerals were determined by electron microprobe analysis (EPMA) using a CAMECA SX-50 electron microprobe, equipped with four wavelength-dispersive spectrometers (WDS) and one energy-dispersive spectrometer (EDS), at IGG-CNR, Padua (Italy). The K α emission lines of ten elements (Na, Mg, Al, Si, K, Ca, Ti, Cr, Mn, Fe) were measured using the following natural and synthetic minerals and oxides as standards: albite (Na), diopside (Si, Ca), orthoclase (K), MgO, Al₂O₃, MnTiO₃, Cr₂O₃ and Fe₂O₃. Working conditions were 20 kV, 20 nA, 10 s for peak and 5 s for the background on each side of the peak.

3.2. Bulk rock compositions

Fourteen rock samples, representative of the main lithologies encountered in and around the deposit, were analysed for major, minor and selected trace elements by X-ray fluorescence (XRF). The samples were prepared as fine powder by means of a Retsch MO agate mortar grinder and a Retsch RS100 vibratory disk mill, equipped with agate disks. The powder samples, fused into beads, were then analysed using a Philips PW2400 XRF wavelength-dispersive sequential spectrometer equipped with a Rh tube at the Department of Geosciences of the University of Padua (Italy). Reference standards were natural geological samples (Govindaraju, 1994). The relative analytical precision is estimated to within $\pm 0.6\%$ for major and minor elements and within $\pm 3\%$ for trace elements. The relative accuracy is within $\pm 0.5\%$ for Si, $\pm 3\%$ for the other major and minor elements, and $\pm 5\%$ for trace elements. Detection limits are better than 0.01 wt% for Al, Mg and Na, 0.2 wt% for Si and 0.005 wt% for Ti, Fe, Mn, Ca, K and P. For trace

elements, the detection limits are 3 ppm for Co, Ni, Cu, Zn, Rb, Sr, Y, Zr, Nb, Th, and U, 5 ppm for Sc, V, Ga, and Pb, 6 ppm for Cr, and 10 ppm for Ba, La, Ce, and Nd.

The geochemistry of seven whole-rock samples was further investigated by inductively coupled plasma mass spectrometry and emission spectroscopy (ICP-MS/ES) analyses, which were performed by Bureau Veritas Mineral Laboratories (Canada). The pulverised rock samples were mixed with LiBO₂/Li₂B₄O₇ flux and fused. The cooled beads were then digested with ACS grade nitric acid. The detection limits for trace elements are: 1 ppm for Be, Sc, Sn, and Ba; 8 ppm for V; 14 ppm for Cr; 0.2 ppm for Co and Th; 20 ppm for Ni; 0.5 ppm for Ga, Sr and W; 0.1 ppm for Y, Zr, Nb, Cs, Hf, Ta, U, La, Ce; 0.3 ppm for Nd.

3.3. U-Th-Pb dating

Thirteen thin sections of magnetite ore were scanned for uraninite crystals by SEM-BSE imaging. Four of these samples showed uraninite grains of sufficient size to allow their chemical analysis by EPMA and successive dating by the U-Th-Pb method. Uraninite compositions were measured at the Department of Earth Sciences of the University of Milan (Italy), using a JEOL JXA-8200 electron microprobe equipped with five WDS and one EDS. An accelerating voltage of 15 kV and a beam current intensity of 20 nA were used. Nine elements were measured by WDS spectrometry using the following X-ray lines: MgK α , SiK α , TiK α , CaK α , CrK α , FeK α , UM β , ThM α and PbM α . The counting time was 60 s for the peak and 30 s for the background for all analysed elements. The standards were olivine (Mg), grossular (Si and Ca), ilmenite (Ti), fayalite (Fe), pure Cr and synthetic UO₂, ThO₂ and PbO. Detection limits for elements relevant to geochronology are 290 ppm for U, and 170 ppm for Th and Pb. Relative errors (relative standard errors) of 0.1%, 0.5% and 0.7% for U, Th and Pb concentrations, respectively, were calculated on the basis of 5 repetitions of the same measurement. However, a more realistic minimum relative error for U, Th and Pb concentrations >7500 ppm is 2% (Cocherie and Albarede, 2001).

Chemical maps were preliminarily acquired on the uraninite grains to assess the presence of chemical zoning. In order to collect a significant amount of data, we performed both single spot analyses and automated traverses. The latter method allowed us to obtain a large number of data points, although the proportion of mixed or poor-quality analyses increased. Thus, prior to calculating ages, we excluded the analyses which showed obvious contaminations, low totals or anomalously low Pb contents, if compared to adjacent points in the same traverse.

The possibility of dating uraninite with EPMA was discussed by Bowles (1990) and calculated ages were demonstrated to be accurate and consistent with independent isotopic measurements (Bowles, 2015; Cross et al., 2011). According to Bowles (2015), the best accuracy is obtained for ages from ~2 Ma to 700–1000 Ma: the lower limit is imposed by the EPMA detection limit of Pb and the upper limit is linked to metamictization of the uraninite crystal lattice, which may lead to Pb loss. Meaningful ages are obtained if the initial concentration of non-radiogenic Pb is negligible and the U-Th-Pb system remained closed after uraninite crystallization. The former assumption is considered to hold true because Pb²⁺ is incompatible in the uraninite crystal structure (Alexandre and Kyser, 2005), whereas the latter assumption needs to be assessed by careful sample examination.

The formula used to calculate the age t (in years) is (Montel et al., 1996):

$$\begin{aligned} \text{Pb} = & 208(\text{Th}/232) \cdot [\exp(\lambda^{232} \cdot t) - 1] \\ & + 206(\text{U}/238.04) \cdot [1 - ({}^{235}\text{U}/{}^{238}\text{U})] \cdot [\exp(\lambda^{238} \cdot t) - 1] \\ & + 207(\text{U}/238.04) \cdot ({}^{235}\text{U}/{}^{238}\text{U}) \cdot [\exp(\lambda^{235} \cdot t) - 1], \end{aligned} \quad (1)$$

where Th and U are the measured concentrations in ppm, λ^{232} , λ^{238} , λ^{235} are the decay constants of ^{232}Th , ^{238}U and ^{235}U , respectively, and $^{235}\text{U}/^{238}\text{U}$ is the bulk Earth's uranium isotopic ratio. The values used in the calculations are: $\lambda^{232} = 4.9475 \cdot 10^{-11} \text{ a}^{-1}$ (Le Roux and Glendenin, 1963); $\lambda^{238} = 1.55125 \cdot 10^{-10} \text{ a}^{-1}$ and $\lambda^{235} = 9.8485 \cdot 10^{-10} \text{ a}^{-1}$ (Jaffey et al., 1971); $^{235}\text{U}/^{238}\text{U} = 0.0072559$ (Hiess et al., 2012). To obtain an initial guess of t we used the formula (modified from Bowles, 2015):

$$t = (1/\lambda^{238}) \cdot \ln \left\{ 1 + \frac{\text{Pb}}{206(\text{U}/238.04) \cdot [1 - (^{235}\text{U}/^{238}\text{U})]} \right\}.$$

Then the difference between the calculated and the measured values of Pb is minimized by least-squares method, varying t . Whenever possible, ages were obtained as weighted averages of several analyses, after outlier rejection based on a modified 2σ set of criteria (Ludwig, 2012).

3.4. Trace elements in magnetite

Trace elements in magnetite were measured by laser-ablation inductively-coupled plasma mass spectrometry (LA-ICP-MS) at the Petrology of the Ocean Crust Laboratory, University of Bremen (Germany), using a high-resolution double-focussing ThermoFinnigan Element2, equipped with a solid-state laser with a wavelength of 193 nm (New Wave UP193). Magnetite grains were analysed on standard thin polished sections using a 35 μm laser spot size, a pulse frequency of 5 Hz, an irradiance at the sample of $\sim 1.3 \text{ GW}/\text{cm}^2$ and an acquisition time of 60 s, comprehensive of 25 s for background measurement. To avoid any risk of contamination on the surface of the rock section, the zone to be investigated was pre-ablated using two laser pulses with 50 μm spot size. The analysed elements (^{25}Mg , ^{29}Si , ^{43}Ca , ^{47}Ti , ^{51}V , ^{53}Cr , ^{55}Mn , ^{57}Fe , ^{59}Co , ^{60}Ni , ^{66}Zn , ^{90}Zr , ^{98}Mo) were measured in low-resolution mode in order to shorten the acquisition time, although preserving high counts per second (cps). We opted for this configuration to avoid deep ablation pits, thus reducing the probability of hitting inclusions or adjacent minerals. The Fe concentration of magnetite as determined by EPMA was used as an internal standard. External standards (reference materials NIST61, BCR-2G and BHVO) were analysed under the same conditions as the samples every 5 to 9 analyses during the same session, in order to check for possible drift. Signal files, reporting intensities (in cps) vs. time, were inspected for possible heterogeneities related to the presence of inclusions and chemical zoning. Integration of the signal and calculation of concentrations were performed with the GeoPro™ software (CETAC Technologies). Detection limits (DL) were calculated on reference materials using the formula:

$$DL_i = [3\sqrt{2}s_{bkgd} / (\bar{X}_{sgl} - \bar{X}_{bkgd})] \cdot C_i,$$

where i is the i^{th} element, s_{bkgd} is the sample standard deviation of the background (in cps), \bar{X}_{sgl} and \bar{X}_{bkgd} are the average signal and the background (in cps) respectively, and C_i is the concentration (in ppm) of the i^{th} element in the reference materials.

The statistical relationships between chemical elements in magnetite were explored by robust principal component analysis (PCA), using the function “pcaCoDa” in the “robCompositions” library for R software (Templ et al., 2011). Robust PCA was preferred to “classical” PCA because it is less sensible to outliers (Filzmoser et al., 2009; Filzmoser and Hron, 2011). Four analyses (out of ninety-four) with V contents below the detection limit were excluded from calculations.

3.5. Geochemical modelling

In an attempt to simulate the genesis of the Cogne deposit in a seafloor hydrothermal model system, fluid-rock interactions were modelled with the EQ3/6 (Version 8.0a) software package (Wolery, 2013), using the database compiled by Klein et al. (2009), which contains thermodynamic properties of minerals and solutes in the 0–400 °C range at the fixed pressure of 500 bar. The database was modified to include revised data for $\text{HCl}_{(\text{aq})}$ (Ho et al., 2001), $\text{NaCl}_{(\text{aq})}$ (Ho et al., 1994), $\text{KCl}_{(\text{aq})}$ (Ho et al., 2000), $\text{FeCl}_{2(\text{aq})}$ and $\text{FeCl}_{(\text{aq})}^+$ (Ding and Seyfried, 1992). The modelling procedure, which in the first steps follows that of Klein et al. (2009), is described below.

First, 1 kg of modern seawater (Table 1; composition from Klein et al., 2009) is speciated at 25 °C and 1 bar. Then, seawater is heated and reacted with 1 g of fresh harzburgite (Table 2) in a closed system to the desired temperature (at $P = 500$ bar), to simulate a downward fluid path towards the reaction zone (Klein et al., 2009). The chosen pressure of 500 bar simulates conditions at ~ 2000 m below seafloor, which do not exceed the reported depth of magma chambers fuelling hydrothermal fields on slow-spreading ridges (~ 3 km; Singh et al., 2006), assuming a 3000-m water column, which is a typical value for modern slow-spreading ridge hydrothermal systems (Edmonds, 2010). All the produced minerals are removed at the end of the run, because in a real fluid pathway they would be left behind by downwelling seawater. A positive effect of this step is to narrow down the f_{O_2} range in following calculations, thus improving the code stability (Wolery and Jarek, 2003). In the successive step, which simulates a reaction zone, 1 kg of the resulting hydrothermal fluid is reacted at 400 °C with an increasing amount of either fresh harzburgite or Fe-gabbro (Table 2) in a closed system (Wolery and Jarek, 2003). We chose the temperature of 400 °C because it maximizes Fe solubility, which is strongly temperature-dependent (Seyfried et al., 2004), and is also compatible with estimates of fluid temperatures in modern subseafloor reaction zones ($T > 375$ °C, Berndt et al., 1989; $T \sim 400$ °C based on the maximum amount of heat that water can carry by buoyancy-driven advection, Jupp and Schultz, 2004 and references therein) and with measured temperatures of modern seafloor vent fluids (e.g., Edmonds, 2010). The reaction path is terminated after the maximum value of dissolved Fe is reached. Finally, the Fe-rich hydrothermal fluid is titrated in a closed system with selected lithologies (Table 2) at 300 °C or 400 °C, in accordance with the temperature range estimated for hydrothermal mineral assemblages by Carbonin et al. (2014). The equilibrium mineral assemblages and the relative abundances of the phases obtained for different water/rock (W/R) ratios are then compared to those observed in the natural rocks. The model does not account for solid solutions, hence, by suppressing Fe-Mg

Table 1
Seawater composition.*

Na ⁺	464.0
Cl ⁻	546.0
HCO ³⁻	2.34
Ca ²⁺	10.2
Mg ²⁺	53.0
K ⁺	9.8
SiO _{2(aq)}	0.11
Fe ²⁺	0.0000015
Al ³⁺	0.000037
SO ₄ ²⁻	28.2
O _{2(aq)}	0.25
pH	7.8

* After Klein et al. (2009).

Table 2
Rock compositions used in thermodynamic modelling.

Rock Type	Fe-gabbro ¹	Dunite ¹	Serp. Dunite ²	Harzburgite ¹	Serp. Harzburgite ²	Pegmatoid serpentinite ³	Troctolite ¹	Serp. Troctolite ⁴
Ox. wt%								
SiO ₂	47.94	40.87	39.24	44.31	39.38	40.97	42.90	37.95
Al ₂ O ₃	12.19	0.00	0.19	0.42	0.59	0.78	9.58	6.12
FeO	18.87	9.77	7.57	8.97	6.61	9.23	9.06	8.44
MgO	4.85	49.35	38.79	45.81	38.37	37.26	32.39	34.73
CaO	13.17	0.00	0.08	0.48	1.69	0.04	5.39	2.87
Na ₂ O	2.99	0.00	0.13	0.00	0.05	0.00	0.67	0.41
H ₂ O	0.00	0.00	13.99	0.00	13.30	11.72	0.00	9.47
Tot.	100.00	100.00	100.00	100.00	100.00	100.00	100.00	100.00

¹ “Artificial” rock.

² Andreani et al. (2014).

³ Sample CDP15, Site 1.

⁴ Sanfilippo et al. (2014).

exchange in secondary phases, it maximizes the extent of magnetite production.

4. Results

4.1. Petrographic features of the magnetite ores and mineral compositions

The Cogne magnetite ore is heterogeneous in terms of texture and gangue mineral assemblage. Three main textural types of magnetite ore are distinguished, which are termed here *nodular*, *fine-grained disseminated* and *vein*.

The nodular ores (Fig. 3a, b) are characterized by mm to cm-sized magnetite crystals in a silicate matrix, giving the rock a macroscopic appearance similar to that of nodular chromitites. The nodular textures show a continuum between three major subtypes, which are termed here *leopard*, *harrisitic* and *massive* subtype, respectively. In the leopard subtype, the magnetite crystals, which mostly consist of aggregates of subgrains, are subrounded and constitute up to 50 vol% of the rock. In the harrisitic subtype, the magnetite crystals form up to 10 cm-long rods, mimicking the texture shown by dendritic olivine in harrisite. In the massive subtype, the magnetite content is as high as 80–90 vol%, but subrounded crystals similar to those of the nodular ores are still recognizable.

The fine-grained disseminated ores consist of bands in the host-rock, which contain variable proportions of sub-millimetric magnetite grains (up to ~70 vol%). The vein ores (Fig. 3c) are cm-thick, dismembered veins composed of magnetite, chalcopyrite and antigorite; the proportion of opaque minerals over the associated silicates is ~50 vol%.

Since the distribution of the different ore types is not uniform across the deposit, we will treat each sampling site separately.

4.1.1. Site 1

The magnetite orebody lies below magnetite-poor (3–6 vol% Mag) serpentinitized mantle harzburgites. The harzburgites show a more or less developed foliation, and are characterized by the presence of lizardite + antigorite + magnetite ± talc pseudomorphs after former olivine and orthopyroxene (distinguished based on the presence of mesh and bastite textures, respectively) and relicts of accessory Mg-Al-rich chromite (Table 3). Magnetite is fine-grained (<20 μm) and Cr-bearing (Carbonin et al., 2014). A detailed description of the mineralogy and conditions of seafloor serpentinitization of these rocks was given in Carbonin et al. (2014; T = 200–300 °C, log *f*_{O₂} = –36 to –30, log ΣS = –2 to –1).

Only nodular ores can be found at this site (Fig. 3a, b). Independently of the ore texture, the gangue mineral assemblage is fairly uniform and comprises, in the order of decreasing abundance,

antigorite, lizardite, forsterite, brucite, clinocllore, carbonates, and Ti-rich chondrodite (Table 3). Antigorite composes > 90 vol% of the matrix between the magnetite crystals. It usually shows an interlocking texture (average grains size = 150 μm), but it can form euhedral, randomly oriented blades when in contact with lizardite or magnetite, forming indented crystal boundaries with the latter mineral (Fig. 4a). This feature was already described in rocks from the western Alps by Debret et al. (2014), who interpreted it as a prograde dissolution texture produced during Alpine subduction metamorphism; however, the antigorite studied by Debret et al. (2014) generally has higher Fe content (up to 8 wt% FeO) than antigorite at Cogne (mostly < 3 wt% FeO). Lizardite forms yellowish aggregates of submicron-sized crystals, which are interstitial between euhedral antigorite and magnetite. The Al₂O₃ content of lizardite (~5 wt%) is systematically higher than that in antigorite (<1 wt%). Forsterite (Fo₉₉) forms up to 50 μm anhedral crystals, usually arranged into elongated aggregates, which replace and seldom form pseudomorphs after antigorite. The forsterite crystals are often altered to fine-grained antigorite along the rim and the fractures. Brucite is of nearly pure Mg-endmember composition and forms subhedral, tabular crystals up to 200 μm in size. Clinocllore forms tabular crystals and intergrowths with antigorite. These intergrowths probably result from the breakdown of Al-rich lizardite. The carbonates (calcite, magnesite, dolomite) form anhedral patches which include antigorite, brucite and fine-grained (<50 μm) anhedral magnetite. Calcite is the most common carbonate and is also present as late veins. Ti-rich chondrodite forms up to 500 μm, colourless to pale yellow, anhedral crystals, which are sometimes surrounded by a corona of olivine. Rare accessory minerals are xenotime, sphalerite, Ni-bearing linnaeite, pyrrhotite and uraninite.

Magnetite-rich (~25 vol%) diopsidites have also rarely been found. In these peculiar rocks, magnetite is interstitial between mm- to cm-sized diopside crystals and coexists with antigorite, andradite and clinocllore. The assemblage antigorite + andradite appears to replace diopside. Samples of this kind were thoroughly described by Carbonin et al. (2014).

4.1.2. Site 2

At this site, the serpentinitized mantle peridotite can be either replaced by fine-grained disseminated magnetite or crosscut by cm-thick magnetite + chalcopyrite + antigorite veins. The disseminated and vein ores are deformed and dismembered into lenses by Alpine deformation, which at small scale results in an anastomosing pattern of mm- to cm-spaced cleavage planes. This deformation is associated with dynamic recrystallization of antigorite and magnetite, the latter forming elongated porphyroclasts.

The disseminations occur as cm-sized magnetite-enriched bands in antigorite serpentinite and typically show relict features

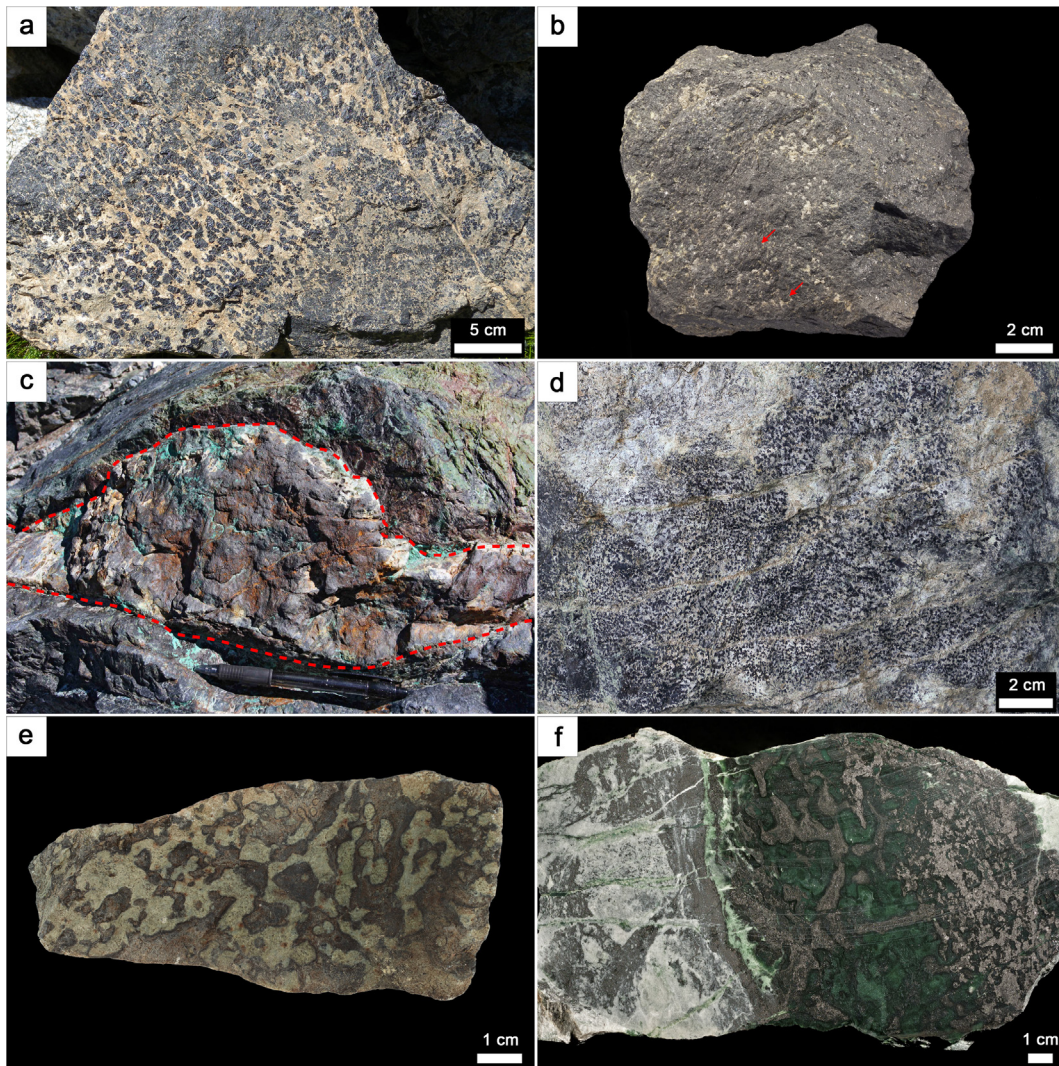


Fig. 3. Typical magnetite ore and rock samples from Site 1 (a, b, e), Site 2 (c) and Site 3 (d, f). a) Nodular ore sample, showing leopard (lower left corner), harristic (cm-sized iso-oriented rods of magnetite in the centre) and massive (upper portion) texture. The light matrix is serpentine (+brucite + olivine). b) Massive ore, with minor serpentine gangue. Arrows indicate rounded magnetite crystals. c) Deformed magnetite (+chalcopyrite + antigorite) vein (outlined by dashed lines) in serpentinized peridotite. Chalcopyrite is completely weathered into Fe-oxyhydroxides and secondary copper minerals. The pen is 14 cm-long. d) Fine-grained leopard ore in diopside gangue. e) Magnetite-poor pegmatoid serpentinite. Note the presence of dark and light interlobate domains. The former are composed of antigorite and minor magnetite, the latter are formed by antigorite only. f) Contact between a magnetite-rich diopside (left) and a pegmatoid serpentinite (right) with amoeboid magnetite-rich domains (light grey) interweaved with magnetite-free domains. Dark antigorite coronae contour the two domains. Magnetite content increases in the right part of the sample, but embayed boundaries are still recognizable. Cut and polished sample.

of the former serpentinized peridotite, i.e., bastites (Fig. 4b) and Mg-Al-rich chromite grains (Fig. 4c, d; Table 3). The Mg-Al-rich chromite grains (Fig. 4d) are anhedral and fractured. They are irregularly altered along the rims and fractures into Fe-rich (~41 wt% FeO) chromite + fine-grained Cr-rich (~4–6 wt% Cr₂O₃, determined by SEM-EDS) chlorite and are mantled by a continuous rim of Cr-bearing magnetite intergrown with antigorite and minor secondary diopside.

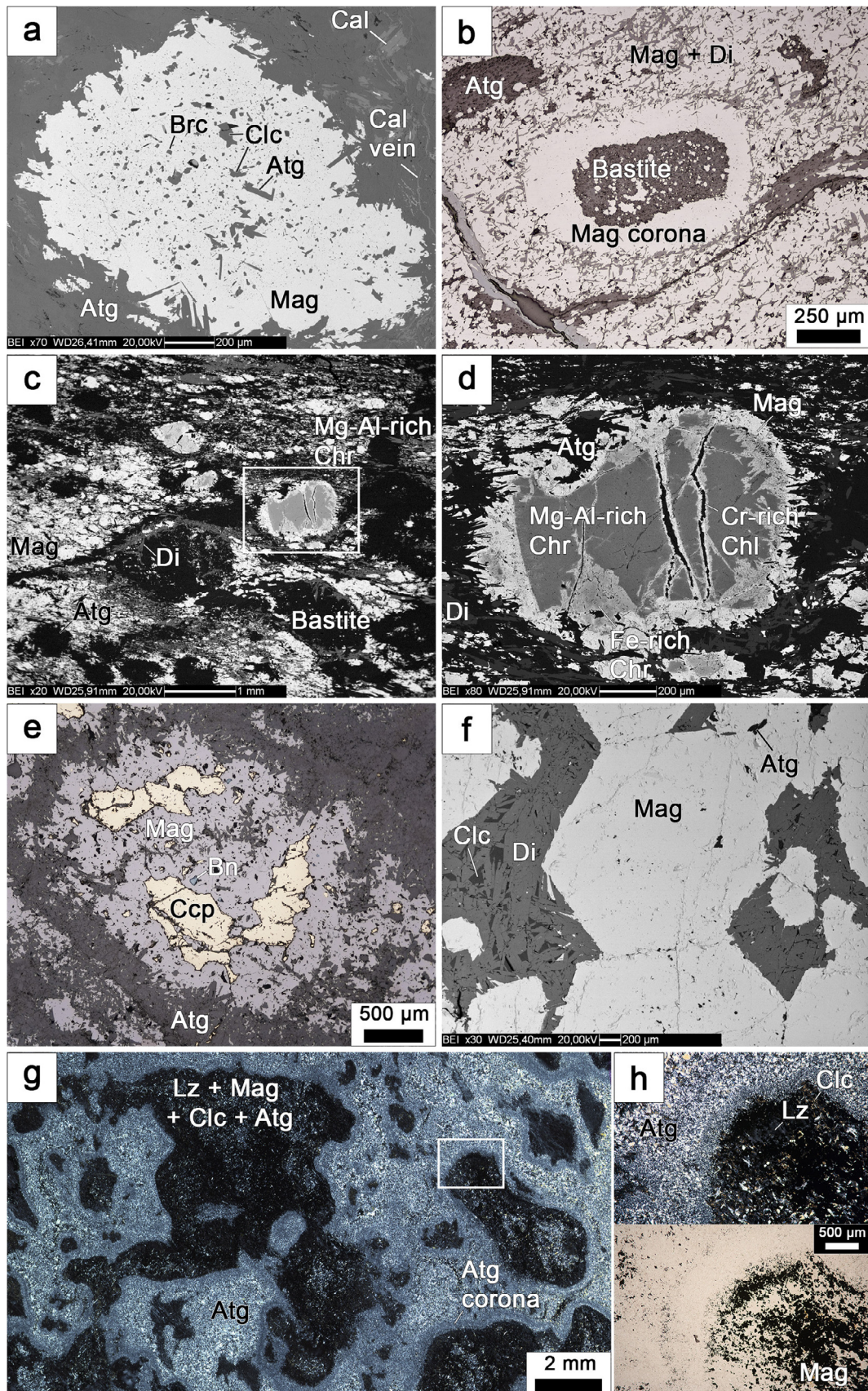
In the vein ores, magnetite forms elongated, millimetric patches with a chalcopyrite core in an antigorite matrix (Fig. 4e). Magnetite shows well developed crystal boundaries towards chalcopyrite, while the contacts to the surrounding antigorite are irregular. The limit between the vein and the host serpentinite is sharp.

In both disseminations and veins, antigorite shows an interlocking texture. When it is in contact to magnetite or lizardite it forms up to 100 μm-long euhedral lamellar crystals, producing typical indented boundaries. A generation of nearly pure diopside (Table 3) always accompanies magnetite mineralization. In magnetite

disseminations, diopside forms up to 400 μm-long isolated needles, intergrown with antigorite (Fig. 4c, d), while in the vein ore, it forms rare aggregates of 10–60 μm long crystals disseminated in the vein selvages. From textural relationships, diopside appears to postdate the formation of bastite pseudomorphs after orthopyroxene in the host serpentinite.

4.1.3. Site 3

At this site, the magnetite ores exhibit nodular textures, but only the leopard and massive subtypes are found. Antigorite is commonly the sole gangue mineral, but the leopard subtype can be characteristically enriched in diopside ± chlorite (Figs. 3d, 4f; Table 3). Antigorite shows an interlocking texture or forms euhedral crystals when in contact to magnetite or diopside. Antigorite veins crosscutting diopside crystals have been observed. Diopside has a nearly pure endmember composition. In the leopard ores, it forms a granofels composed of mm- to cm-sized subhedral crystals, which include subhedral millimetric magnetite. A late gener-



ation of smaller subhedral crystals (<50 μm) fills the interstices between larger grains. The diopside crystals may show patchy or concentric oscillatory zoning, determined by slight variations in Fe content. Textural relationships indicate that diopside formed during a late stage of magnetite growth (Fig. 4f), which was then locally overprinted by antigorite. Veins made up of euhedral diopside in a matrix of lizardite \pm chlorite are commonly observed. Clinocllore is found in diopside-rich leopard ores and has variable Mg# ratios and Al contents (Table 3): the Al-rich variety is found as large (up to 1 mm) subhedral tabular crystals associated with diopside and magnetite; the Al-poor clinocllore is fine-grained and fills the interstices between larger clinocllore and diopside crystals. Calcite is found as interstitial material between diopside crystals and as late veins. Rare accessory minerals are andradite, uraninite, talc and apatite.

4.1.4. Inclusions in magnetite

The magnetite crystals can be rich in mineral inclusions, which, in the largest poikiloblasts, are typically concentrated in their cores (Fig. 4a).

At Site 1, the most common inclusions are clinocllore and brucite lamellae (Table 3), often oriented along magnetite (111), anhedral calcite, anhedral sphalerite, rare anhedral pyrite, rare lizardite and forsterite, and very rare euhedral uraninite and apatite. Antigorite inclusions are often present in the outermost zones of the magnetite crystals. Composite inclusions made up of clinocllore + brucite or, rarely, clinocllore + calcite are also observed.

At Site 2, the most abundant inclusions are euhedral antigorite and anhedral sulphides. The sulphides consist of fine lamellar chalcopyrite–cubanite intergrowths and unmixed “bornite solid solution” grains, composed of lamellar intergrowths of bornite and chalcocite. Also present are pyrrhotite, which shows exsolution of Co-rich pentlandite, and sphalerite. Other minor included minerals are lamellar clinocllore and anhedral andradite.

At Site 3, the inclusions are mainly composed of clinocllore, which can be associated with rare andradite (Table 3) and very rare diopside and uraninite; antigorite inclusions are only present near the rims of the magnetite crystals.

4.2. Petrography of peculiar host rocks at sites 1 and 3

At sites 1 and 3, serpentinites showing a pegmatoid texture are associated with the magnetite ore and can be variably enriched in magnetite. In the barren rocks (Fig. 3e), cm-sized amoeboid domains made of dominant euhedral coarse-grained (50–300 μm) antigorite that replaces yellow, fine-grained (sub-micron sized) lizardite are interweaved with domains composed of mesh textured antigorite + lizardite and very fine-grained magnetite (magnetite I) lining the rims of the mesh. Lizardite is Al-rich in both domains (Raman peak at 382–385 cm^{-1} , indicating Al

substitution for Si in the tetrahedral sites; Groppo et al., 2006). Coronae of interlocking antigorite line the boundaries between the two domains. In magnetite-enriched rocks, the early fine-grained (<30 μm), usually euhedral magnetite (I) associated with Al-rich lizardite (Table 3) is overgrown by a new generation of coarser-grained, subhedral to anhedral disseminated magnetite (magnetite II) + euhedral antigorite + lamellar clinocllore. Clinocllore probably forms as consequence of the transformation of Al-rich lizardite to Al-poor antigorite, since its content is proportional to the amount of antigorite that replaces lizardite. The two magnetite generations have similar major element compositions (Table 3). Possible variations in trace element compositions could not be determined because of the small crystal size of magnetite I. Magnetite II can completely replace the lizardite-rich domains, but the amoeboid shape of the domains and the antigorite coronae are usually preserved (Figs. 3f, 4g, h). On the contrary, the antigorite domains and coronae show only scarce anhedral magnetite (Fig. 4g, h). A magnetite-rich diopsidite, composed of dominant fine-grained diopside (<50 μm), subordinate magnetite and minor euhedral antigorite (<150 μm ; Fig. 3f; Tables 3 and 4), has been observed in contact with the magnetite-rich pegmatoid serpentinite.

4.3. Bulk rock geochemistry

Bulk rock compositions are reported in Table 4. The magnetite-poor ($\text{Fe}_2\text{O}_3 < 8.5 \text{ wt}\%$) serpentinitized peridotites have major and trace element concentrations typical for refractory peridotites (cf. Andreani et al., 2014; Bodinier and Godard, 2003; Niu, 2004; Paulick et al., 2006), such as low Al_2O_3 (~1–3 wt%) and TiO_2 (0.02–0.1 wt%), high Ni (~1400–2800 ppm) and Cr (~1900–2600 ppm) and low Co/Ni ratio (~0.05–0.07). The Cu and Zn contents (~20 and ~40–50 ppm, respectively) are also typical for upper mantle peridotites (cf. O'Neill and Palme, 1998; Niu, 2004; Fouquet et al., 2010). The pegmatoid serpentinites have variable Al_2O_3 (~0.8–2.6 wt%), Fe_2O_3 (~4.5–10 wt%), Ni (~500–2000 ppm), and Cr (~10–2700 ppm) contents and Co/Ni ratios (~0.05–0.2). However, Cu and Zn show very little variation (~20 and ~30–40 ppm, respectively).

The magnetite-enriched ($\text{Fe}_2\text{O}_3 > 28 \text{ wt}\%$) serpentinites have different compositions reflecting their distinct host rocks. The magnetite-rich pegmatoid serpentinite has a high Al_2O_3 content (~2 wt%) and a high Co/Ni ratio (~0.4), but low Ni, Cr, Cu and Zn contents (~280, ~10, ~70, ~60 ppm, respectively). The fine-grained disseminated ore has Al_2O_3 , Cr and Ni contents (~1 wt%, ~2200, ~1200 ppm, respectively) in the same range as the magnetite-poor serpentinitized peridotites, but has higher Cu and Zn contents (~200 and ~120 ppm, respectively) and a higher Co/Ni ratio (~0.1). With further increase in magnetite content, the concentrations of Cr (~1300 ppm) and Ni (~240 ppm)



Fig. 4. Microstructural features in Cogne rocks. a) Magnetite poikiloblast in leopard ore from Site 1, showing indented boundaries with antigorite. Inclusions in magnetite are clinocllore (usually anhedral), brucite (small and euhedral) and antigorite (large euhedral crystals). Gangue is antigorite with minor calcite, which forms late impregnations and thin veins. SEM-BSE image. b) Nearly massive fine-grained disseminated ore from Site 2. Magnetite (white) is associated with acicular diopside (grey) and forms a corona around an antigorite (dark grey) bastite. Reflected plane-polarized light. c) Fine-grained disseminated ore from Site 2. Magnetite (white), antigorite (black) and diopside (medium grey) replace former silicates, but bastite sites (round black areas) and Mg-Al-rich chromites (framed; see Fig. 4d for a close-up) are still preserved. SEM-BSE image. d) Mg-Al-rich chromite crystal (medium grey), partly altered along the rims and fractures into Fe-rich chromite (light grey) + Cr-rich chlorite (black) and mantled by magnetite, intergrown with antigorite (black) and diopside (dark grey). e) Magnetite + chalcopyrite patch associated with antigorite in a dismembered vein from Site 2. Bluish inclusions in magnetite are bornite. Antigorite occurs both within and around the magnetite, forming indented boundaries with it. Reflected plane-polarized light. f) Euhedral magnetite crystals in a diopside-rich portion of a leopard ore sample from Site 3. Diopside forms randomly-oriented subhedral prismatic crystals (medium grey) with interstitial antigorite (dark grey). Black mineral included in magnetite or interstitial between diopside crystals (right) is clinocllore. SEM-BSE image. g) Serpentinized pegmatoid ultramafic rock from Site 3 (see Fig. 3f), showing interlobate domains separated by coronae structures. Transmitted light, crossed polars. h) Enlargement of framed area in c). Light-coloured domain (upper left) is composed of coarse-grained interlocking antigorite; dark domain (right) is made up of isotropic lizardite, clinocllore (anomalous brown interference colour), antigorite (white-light grey) and magnetite (opaque). Fine-grained interlocking antigorite lines the boundary between the two domains. Transmitted light, crossed polars (upper) and plane polarized light (lower). Mineral abbreviations – Mag: magnetite; Atg: antigorite; Clc: clinocllore; Brc: brucite; Cal: calcite; Di: diopside; Lz: lizardite; Ccp: chalcopyrite; Bn: bornite; Chr: chromite; Chl: chlorite. (For interpretation of the references to colour in this figure legend, the reader is referred to the web version of this article.)

Table 4
Bulk chemistry of representative rock types.

Location	Site 1	Site 1	Site 1	Site 1	Site 1	Site 1	Site 2	Site 2	Site 2	Site 3	Site 3	Site 3	Site 3	Site 3
Sample	LIC1B	CDP15	MZ18	LIC12	LIC14	LIC15	ECL1	MZL3	CRY1	LAR4	LAR2-1	LAR2-2	CGN3	CGN8
Rock type	Serpentinized peridotite	Pegmatoid serpentinite	Pegmatoid serpentinite	Serpentinized peridotite	Nodular ore	Nodular ore	Fine-grained disseminated ore	Nearly massive fine-grained disseminated ore	Vein ore	Serpentinized peridotite	Mag-rich pegmatoid serpentinite	Mag-rich diopside	Di-rich nodular ore	Nodular ore
Mineral assemblage	Atg, Mag, sulph.	Atg, Lz, Mag	Atg, Lz, Mag, sulph.	Atg, Lz, Mag, Tic, Mg-Al-rich Chr, sulph.	Mag, Atg, Fo, Brc, Clc, Lz, Ti-rich Chn, sulph.	Mag, Atg, Cal, Clc, Brc, Lz	Mag, Atg, Di, Lz, Mg-Al-rich Chr, Chl, sulph.	Mag, Di, Atg, Lz, sulph.	Mag, Atg, Ccp, sulph.	Atg, Mag, Clc, Lz, Cal, sulph.	Atg, Mag, Lz, Clc, Di	Di, Mag, Atg	Mag, Di, Clc, Atg, Cal, Adr	Mag, Atg, Clc, Lz, Adr, Di
<i>Ox. wt%</i>														
SiO ₂	41.95	40.22	40.92	39.54	22.39	20.51	32.20	9.08	24.65	39.10	33.15	42.40	6.52	10.06
TiO ₂	0.02	0.03	0.03	0.02	0.06	0.02	0.04	0.01	0.04	0.10	0.03	0.02	0.02	0.02
Al ₂ O ₃	1.04	0.77	2.59	1.01	0.62	1.08	0.92	1.15	0.43	2.67	2.31	0.27	0.86	0.31
Fe ₂ O ₃	5.46	10.07	4.47	8.32	41.05	47.36	31.10	79.89	43.51	4.95	28.04	21.44	85.73	78.71
MgO	38.31	36.58	37.91	37.61	28.22	21.07	25.72	5.03	22.39	33.42	30.69	16.01	3.90	9.17
MnO	0.11	0.16	0.18	0.10	0.31	0.31	0.17	0.30	0.20	0.16	0.17	0.17	0.35	0.40
CaO	0.26	0.04	0.04	0.02	0.11	2.21	2.63	3.01	0.04	5.85	0.14	18.19	1.50	0.03
Na ₂ O	0.04	0.03	0.03	0.03	0.02	0.02	0.03	0.01	0.02	0.03	0.04	0.02	0.02	0.01
K ₂ O	0.01	0.01	0.01	0.01	0.01	0.01	0.01	0.01	0.00	0.01	0.01	0.01	0.01	0.01
P ₂ O ₅	0.01	0.01	0.01	0.01	0.02	0.01	0.01	0.01	0.01	0.01	0.01	0.01	0.02	0.01
LOI	12.19	11.51	12.63	12.57	6.88	7.09	7.09	0.01	6.75	13.21	5.18	0.72	0.21	0.32
Total	99.40	99.42	98.83	99.25	99.68	99.68	99.91	98.51	98.02	99.50	99.77	99.27	99.13	99.04
<i>ppm</i>														
Be*	–	–	–	<1	<1	–	1	–	–	–	<1	<1	<1	<1
S*	–	–	–	1800	<200	–	3500	–	–	–	<200	<200	<200	<200
S	47	<10	23	1044	228	179	881	169	3068	821	118	103	14	<10
Sc*	–	–	–	6	<1	–	6	–	–	–	2	1	<1	<1
Sc	18	12	22	9	9	<5	<5	<5	10	<5	6	<5	9	13
V*	–	–	–	26	<8	–	31	–	–	–	20	12	<8	<8
V	27	5	57	26	13	12	37	32	51	41	20	14	11	11
Cr*	–	–	–	2395	<14	–	2196	–	–	–	<14	<14	21	<14
Cr	2100	12	2668	2580	12	10	2199	1256	73	1850	13	10	10	13
Co*	–	–	–	117.4	236.8	–	97.8	–	–	–	105.8	72.3	260.9	295.2
Co	76	111	88	133	330	321	129	139	124	96	145	95	407	436
Ni*	–	–	–	2403	93	–	1005	–	–	–	275	97	110	42
Ni	1401	531	1927	2727	97	11	1168	239	477	1338	352	105	113	45
Cu	19	15	18	17	34	27	194	217	13670	20	66	76	45	38
Zn	41	34	40	47	76	103	120	115	131	38	63	38	83	84
Ga*	–	–	–	0.8	1.3	–	<0.5	–	–	–	8.3	2.0	3.5	0.8
Ga	<5	7	8	<5	<5	8	<5	45	<5	7	15	<5	13	<5
Rb*	–	–	–	<0.1	<0.1	–	<0.1	–	–	–	0.1	<0.1	<0.1	<0.1
Rb	6	7	5	7	<3	7	15	<3	8	6	8	17	8	8
Sr*	–	–	–	<0.5	1.3	–	1.0	–	–	–	<0.5	12.4	1.8	0.6
Sr	7	5	5	4	6	81	6	5	7	100	6	18	8	<3
Y*	–	–	–	0.5	0.5	–	0.2	–	–	–	1.0	3.4	0.5	0.4
Y	<3	<3	<3	<3	<3	<3	<3	<3	<3	<3	<3	<3	13	10
Zr*	–	–	–	3.4	5.8	–	0.7	–	–	–	1.9	2.8	1.0	0.8
Zr	9	15	10	9	16	13	9	13	11	14	9	12	9	10
Nb*	–	–	–	<0.1	0.6	–	<0.1	–	–	–	<0.1	0.9	0.4	<0.1
Nb	<3	<3	<3	<3	<3	<3	<3	<3	<3	<3	<3	<3	<3	<3
Sn*	–	–	–	<1	<1	–	<1	–	–	–	<1	<1	<1	<1
Cs*	–	–	–	<0.1	<0.1	–	<0.1	–	–	–	<0.1	<0.1	<0.1	<0.1
Ba*	–	–	–	1.0	<1	–	<1	–	–	–	1.0	3.0	<1	<1
Ba	<10	<10	11	<10	<10	<10	<10	<10	<10	15	<10	<10	<10	<10
Hf*	–	–	–	<0.1	0.2	–	<0.1	–	–	–	<0.1	0.1	<0.1	<0.1

Table 4 (continued)

Location Sample	Site 1 CDP15	Site 1 MZ18	Site 1 LIC12	Site 1 LIC14	Site 1 LIC15	Site 2 ECL1	Site 2 MZL3	Site 2 CRK1	Site 3 LAR4	Site 3 LAR2-1	Site 3 LAR2-2	Site 3 CGN3	Site 3 CGN8
Rock type	Serpentinized peridotite	Pegmatoid serpentinite	Serpentinized peridotite	Nodular ore	Nodular ore	Fine-grained disseminated ore	Nearly massive fine-grained disseminated ore	Vein ore	Serpentinized peridotite	Mag-rich pegmatoid serpentinite	Mag-rich diopsidite	Di-rich nodular ore	Nodular ore
Mineral assemblage	Atg, Mag, sulph.	Atg, Lz, Mag, Tlc, Mg-Al-rich Chr, sulph.	Atg, Lz, Mag, Tlc, Mg-Al-rich Chr, sulph.	Mag, Atg, Fo, Brc, Clc, Lz, Ti-rich Chr, sulph.	Mag, Atg, Cal, Clc, Brc, Lz	Mag, Atg, Mg-Al-rich Chr, Chl, sulph.	Mag, Di, Atg, Lz, sulph.	Mag, Atg, Ccp, sulph.	Atg, Mag, Clc, Lz, Cal, sulph.	Atg, Mag, Lz, Clc, Di	Di, Mag, Atg	Mag, Di, Clc, Atg, Cal, Adr	Mag, Atg, Clc, Lz, Adr, Di
Ta*	-	-	<0.1	<0.1	-	<0.1	-	-	-	<0.1	<0.1	<0.1	<0.1
W*	-	-	1.1	4.0	-	<0.5	-	-	-	<0.5	<0.5	<0.5	<0.5
Pb	11	9	33	15	9	9	<5	18	14	27	22	10	<5
Th*	-	-	<0.2	0.9	-	<0.2	-	-	-	0.3	0.5	<0.2	<0.2
Th	9	9	<3	12	11	6	10	10	4	<3	8	14	12
U*	-	-	<0.1	2.9	-	<0.1	-	-	-	1.3	2.0	0.8	2.4
U	9	4	<3	4	<3	4	<3	6	<3	<3	3.3	<3	<3
La*	-	-	0.9	0.4	-	0.2	-	-	-	0.8	<10	<10	0.3
La	<10	<10	<10	<10	<10	<10	<10	<10	<10	<10	<10	<10	<10
Ce*	-	-	0.7	0.6	-	0.1	-	-	-	0.9	5.8	1.1	0.7
Ce	<10	<10	<10	<10	<10	16	<10	<10	10	11	<10	<10	<10
Nd*	-	-	0.4	0.7	-	<0.3	-	-	-	0.3	3.8	0.7	0.4
Nd	28	20	23	19	17	22	27	24	17	18	29	22	27

- = not determined.

Mineral abbreviations not used before – Adr: andradite; Chn: chondrodite; Fo: forsterite; Tlc: talc; sulph: sulphides; * element concentrations measured by ICP-MS.

decrease, but the Co/Ni ratio increases (~0.6). The magnetite vein ore ($\text{Fe}_2\text{O}_3 \sim 44 \text{ wt}\%$) has low Ni (~500 ppm) and Cr (~70 ppm) contents and an intermediate Co/Ni ratio (~0.3). Moreover, it exhibits moderately high Zn (130 ppm) and the highest Cu content (~14,000 ppm), which reflects the presence of chalcopyrite. The magnetite-rich diopsidite ($\text{Fe}_2\text{O}_3 \sim 21 \text{ wt}\%$) has a trace element composition similar to that of the pegmatoid serpentinite it is in contact with, but it has a higher Co/Ni ratio (~0.9).

In the nodular ores, the SiO_2 and MgO contents are inversely proportional to the amount of magnetite present. The Al_2O_3 and CaO concentrations are variable and reflect the different relative abundances of clinocllore and diopside (or carbonates), respectively. The TiO_2 content is generally low (0.02 wt%), but in the ore from Site 1 it can be slightly higher (~0.06 wt%), consistently with the presence of Ti-rich chondrodite. The nodular ores are virtually Cr-free (~10 ppm), have low Ni (~10–110 ppm) and relatively high Co (~320–440 ppm) contents, which translate into the highest observed Co/Ni ratios (~3–30). Moreover, compared to serpentinized peridotites and pegmatoid serpentinites, they show somewhat higher Cu and Zn (~30–50 ppm and ~80–100 ppm, respectively). The nodular ores, the magnetite-rich pegmatoid serpentinite and the magnetite-rich diopsidite share significant U and Th contents, which reach the maximum values at Site 1 (U = 2.9 ppm; Th = 0.9 ppm). In both magnetite-poor and magnetite-enriched serpentinized mantle peridotites, U and Th contents are below the detection limits of ICP-MS analysis (<0.01 and <0.02 ppm, respectively).

The relationships between magnetite enrichment, Co/Ni ratio and Cr content are shown in Fig. 5. Magnetite enrichment is generally accompanied by an increase in the Co/Ni ratio, but shows no correlation with the Cr content. In particular, the Cr content is very low (<30 ppm) in the nodular ores, in the diopsidites and in most pegmatoid serpentinites (both magnetite-poor and magnetite-enriched) and is higher (Cr > 1200 ppm) in both barren and magnetite-enriched serpentinites after peridotites.

4.4. Age of the deposit

The high U (+Th) contents in nodular ores from Site 1 and Site 3 can be attributed to the presence of uraninite inclusions in magnetite. Uraninite forms anhedral to euhedral cuboctahedral crystals, ranging in size from ~1 to 40 μm (Fig. 6a–c, e, g). Textural evidence suggests that uraninite and magnetite (+clinocllore) were contemporaneous (Fig. 6b, g). The compositions of the uraninite crystals are reported in Table 5. The U/Th ratios are variable (3–21), especially at Site 1, where both the highest and the lowest Th contents were measured. The FeO and CaO concentrations are relatively high (FeO = 0.8–4.9 wt%; CaO = 0.06–1.2 wt%), but they are unrelated to PbO contents, which excludes late-stage alteration (Alexandre and Kyser, 2005). Excitation of the host magnetite within the microprobe interaction volume could explain the presence of Fe in the analyses. On the contrary, the Ca content is considered to be primary and ascribed to lattice-bound substitutions of Ca for U. A less than 1 μm -thick, U-rich rim is sometimes observed in uraninite crystals (Fig. 6e), and is ascribed to partial alteration.

The U-Th-Pb ages calculated for a group of three small (<10 μm) uraninite grains from Site 1 (Fig. 6a–c) are plotted in Fig. 6d. Due to the small grain size, only single-spot analyses were acquired. The weighted average age is $161.8 \pm 3.5 \text{ Ma}$ (MSWD = 0.51). Fig. 6f shows the ages obtained for an aggregate of zoned grains from Site 1 (Fig. 6e). The crystals have a U-rich rim, which testifies for partial alteration. Therefore, we only considered sixteen analyses that form a plateau for PbO, UO_2 and ThO_2 concentrations (Fig. 7). The weighted average age for the plateau, after rejecting two

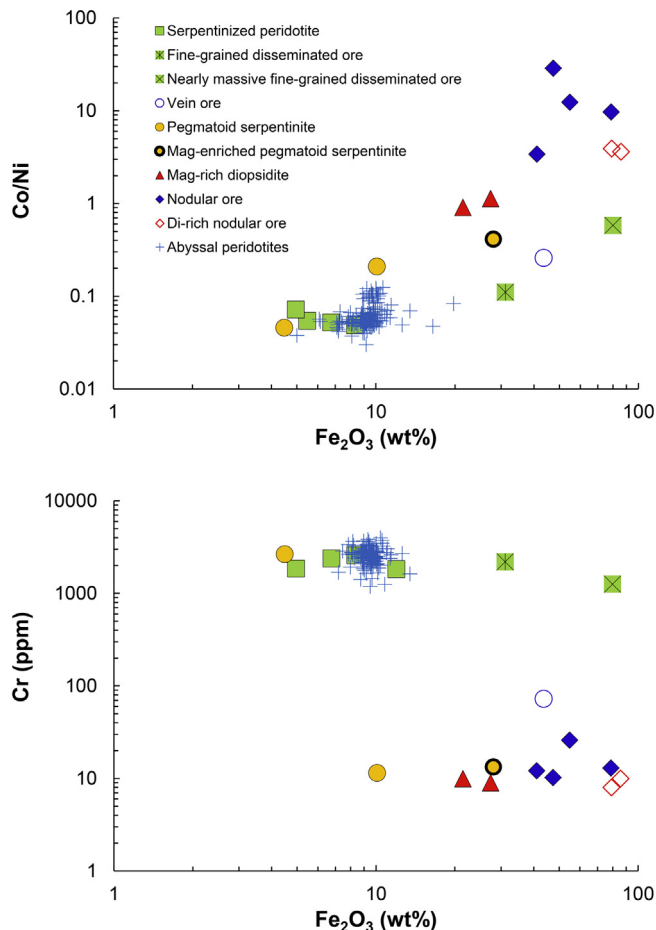


Fig. 5. Covariation of Co/Ni ratio and Cr content vs Fe_2O_3 content in Cogne rocks and ores (this work and Carbonin et al., 2014). Data for abyssal peridotites after Niu (2004), Paulick et al. (2006), Andreani et al. (2014) are shown for comparison.

outliers, is 150.8 ± 2.0 Ma (MSWD = 1.03). The weighted average age calculated for a big (~ 40 μm), unzoned uraninite crystal from Site 3 (Fig. 6g), which is intergrown with magnetite and contains chlorite, is 151.9 ± 1.4 Ma (MSWD = 0.91) (Fig. 6h). Also in this case only plateau PbO values were considered (Fig. 7). The two age determinations that yield the lowest uncertainties and best MSWD values (i.e., close to unity) are within errors of each other and are considered to be the most reliable. However, considering the limited age scatter, it is reasonable to combine all the data into a single age determination, which yields a value of 152.8 ± 1.3 Ma (MSWD = 1.3; Fig. 6i).

4.5. Geochemistry of Cogne magnetite

The compositions of the Cogne magnetites are reported in Tables 3 and 6. The magnetites show significant substitutions of Fe by Mg and Mn (Fig. 8). The concentrations of these metals are the highest at Site 1 (median = $\sim 24,100$ ppm and ~ 5000 ppm, respectively). Concentrations of Ca, Si, Mo, Zr and Cr are generally below or close to the ICP-MS detection limits; only magnetite forming the disseminated ore from Site 2 has significant Cr contents, which can be as high as ~ 150 ppm. Among the other trace elements, the concentrations of Ni, Co, Ti, and Zn are generally an order of magnitude higher than those of V (Fig. 8). The highest concentrations of Co are found at Site 1 (median = ~ 570 ppm), whereas the lowest concentrations are in magnetite in disseminated ore from Site 2 (median = ~ 80 ppm). In spite of across-site

variations, the Co content is fairly constant in magnetite from the same sample. The Ti content is the highest in magnetite from disseminated ore from Site 2 (median = ~ 570 ppm) and the lowest in magnetite from diopside-rich rocks from Site 1 and Site 3 (median = ~ 60 ppm). The Ni and V contents are highest in magnetite from the magnetite-rich pegmatoid serpentinite (median = ~ 670 ppm and ~ 60 ppm, respectively). The lowest Ni and V contents are observed in Site 1 ore (median = ~ 80 ppm) and in vein magnetite (median = ~ 6 ppm), although in the latter both elements are highly variable. The Zn contents show minor variability: the highest values are found in the vein magnetite (median: ~ 160 ppm) and the minimum values are found in magnetite from Site 3 (median: ~ 80 ppm).

Robust PCA indicates that the two first principal components (PC1 and PC2) can explain 97% of the variability of the magnetite compositional data and thus can adequately be used to describe the various magnetite populations. As shown by the loading plot (Fig. 9), Mg, Mn, Co and Zn are highly correlated, while Ni is anti-correlated and V and Ti vary independently from the other elements. In the PC1 vs. PC2 plot, one cluster of samples, which encompasses the magnetites in the nodular ores from Site 1 and Site 3 and the magnetite-rich diopsidite, is characterized by the highest (Mg, Mn, Co, Zn)/Ni ratios. High Ni contents are instead distinctive of magnetite in disseminated ore from Site 2 and in magnetite-rich pegmatoid serpentinite from Site 3 (Fig. 8). These high-Ni magnetites form two distinct groups, in which high Ni is associated with high Ti (and Cr) and high V, respectively. Vein magnetites, having a very variable Ni and low overall V, plot in an intermediate position between high-Ni and low-Ni magnetites. When plotted on the Zn vs. Co plane (Fig. 10), most of the magnetites show a nearly constant Zn/Co ratio of ~ 0.28 . Magnetites in the veins and in the fine-grained disseminated ore from Site 2 have higher Zn/Co ratios (~ 1).

4.6. Thermodynamic modelling

We attempted to reproduce the mineral assemblages observed at Cogne in a model seafloor hydrothermal system. The fluids produced by interaction at 400 $^\circ\text{C}$ of modified seawater with harzburgite and Fe-gabbro (Table 2), respectively, provide two potential endmember compositions for fluids circulating in and reacting with the original oceanic substrate rocks. Harzburgite composes the uppermost part of the Cogne deposit and is the most common type of abyssal peridotite (Mével, 2003). Fe-gabbro is the most Fe-rich rock that can be found in the ophiolitic units of southern Valle d'Aosta (Benciolini et al., 1988; Bocchio et al., 2000; Dal Piaz et al., 2010; Polino et al., 2014) and it can be an efficient source of iron if altered at high temperature. Based on our calculations, dissolved Fe in the harzburgite-reacted fluid (Fig. 11a) increases from W/R ~ 1 to W/R ~ 7 where it reaches a maximum value of ~ 11 mmol/kg (604 ppm). The increase in Fe concentration follows the pH decrease that is in turn controlled by hydrolysis of mantle orthopyroxene, which is much more reactive than olivine at 400 $^\circ\text{C}$ (Charlou et al., 2002). In general, the Fe-gabbro-reacted fluids are more acidic and more Fe-rich. The Fe concentration is up to one order of magnitude higher (Fig. 11b), reaching a maximum value of ~ 26 mmol/kg (1439 ppm) at W/R ~ 80 . Such a high dissolved Fe content again reflects a pH minimum, which immediately follows the total breakdown of plagioclase. This is consistent with experimental evidence that plagioclase alteration to Mg-silicates (chlorite, epidote, talc) by seawater at 400 $^\circ\text{C}$ and high W/R buffers pH to low values (Seyfried, 1987; Seyfried et al., 2010). Other major differences between the two fluid types at their Fe peak concern the concentrations of Mg and Si, which are about one order of magnitude lower and two order of magnitude higher, respectively, in the Fe-gabbro-reacted fluid. The high W/R ratios required to

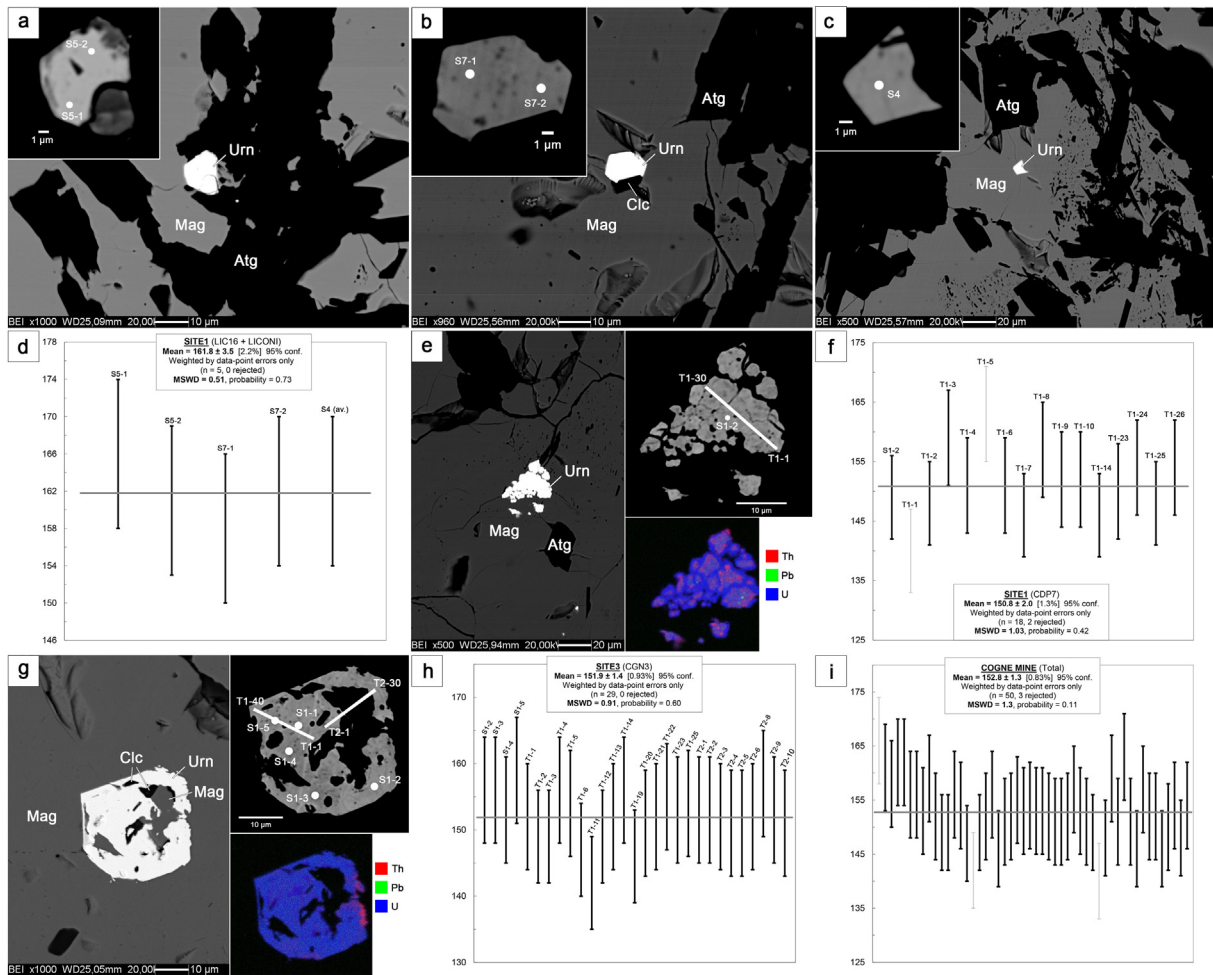


Fig. 6. Uraninite microstructural features and U-Th-Pb dating. a–d) Uraninite (Urn) in Site 1 leopard ore and related dating [b) and c) from the same ore sample], e, f) Aggregate of uraninite crystals in Site 1 leopard ore and related dating. Chemical map shows a U-rich rim. g, h) Inclusion-rich (magnetite, dark grey; clinocllore, black) uraninite crystal in Site 3 leopard ore and related dating. The chemical map reveals a homogeneous composition. i) Combination of all single-spot ages. SEM-BSE images and EPMA chemical maps. Geochronological data plotted using ISOPLLOT (v. 3.75) Visual Basic add-in for Excel® (Ludwig, 2012). MSWD: mean square of weighted deviates.

maximize the Fe contents could potentially be achieved in a highly fractured substrate, such as at the foot wall of a detachment fault in an oceanic core complex (e.g., McCaig et al., 2007).

The harzburgite-reacted and Fe-gabbro-reacted fluids carrying the maximum dissolved Fe were further reacted at either 300 °C or 400 °C with the different lithologies listed in Table 2. We considered temperatures ≥ 300 °C to account for the ubiquitous presence of antigorite (predominant at $T > 300$ °C; Evans, 2004, 2010) in all ore assemblages at Cogne and because these high temperatures disfavour substitution of Fe for Mg in minerals (especially in brucite; Klein et al., 2009), thus accounting for the very high $100 \cdot \text{Mg}/(\text{Mg} + \text{Fe})_{\text{mol}}$ ratios ($\text{Mg}\# > 90$) of gangue minerals in the Cogne deposit (Table 3). Moreover, at the high temperatures considered, and especially at high W/R ratios, the thermodynamic properties of the very Mg-rich gangue minerals are well approximated by their Mg endmembers, hence neglecting solid solutions can be considered to be a minor problem. The only mineral phase that significantly deviates from the ideal composition is lizardite, which is always Al-rich (Table 3). However, textural evidence indicates that lizardite is a minor relict phase that was formed during an early serpentinization event and rarely survived the successive higher temperature ore-forming process (cf. Section 4.1). Accounting for the presence of Al-rich lizardite would not have significantly influenced the modelling of the fluid-rock system at high temperature.

The mineral assemblages produced by hydrothermal fluid-rock interactions are shown in Fig. 12. Magnetite is stable for both fluids over the whole considered W/R range at both 300 °C and 400 °C (with the exception of fresh troctolites reacting with harzburgite-reacted fluid at 300 °C). Under *rock-dominated conditions* ($W/R < 1$), the final alteration mineral assemblages are similar for both fluids: forsterite and brucite are generally formed in addition to magnetite, but their stability is dependent on temperature, with forsterite being stable at higher temperature (Fig. 12b, d) than brucite (Fig. 12a, c). Fayalite is predicted to form at both 300 °C and 400 °C in fresh troctolites and pegmatoid serpentinites. The presence of pure fayalite may be an artefact induced by neglecting solid solutions in olivine. Clinocllore is present in all mineral assemblages at 400 °C (with the exception of the model of a fresh dunite reacting with harzburgite-reacted fluid), but at 300 °C it forms in abundant quantities only in troctolites (both fresh and serpentinized) and pegmatoid serpentinites. Diopside is abundant only in Ca-rich rocks, i.e., harzburgites and troctolites (Table 2), and in troctolites it is associated with tremolite. In these rocks also minor anhydrite forms. At 300 °C in fresh harzburgites and serpentinized dunites the diopside is soon destabilized and the liberated Mg and Si combine with dissolved Al to form clinocllore. At higher temperatures this reaction is limited to higher W/R ratios. Some phlogopite is produced during alteration of fresh troctolites. At *intermediate W/R ratios*, diopside disappears at both 300 °C and

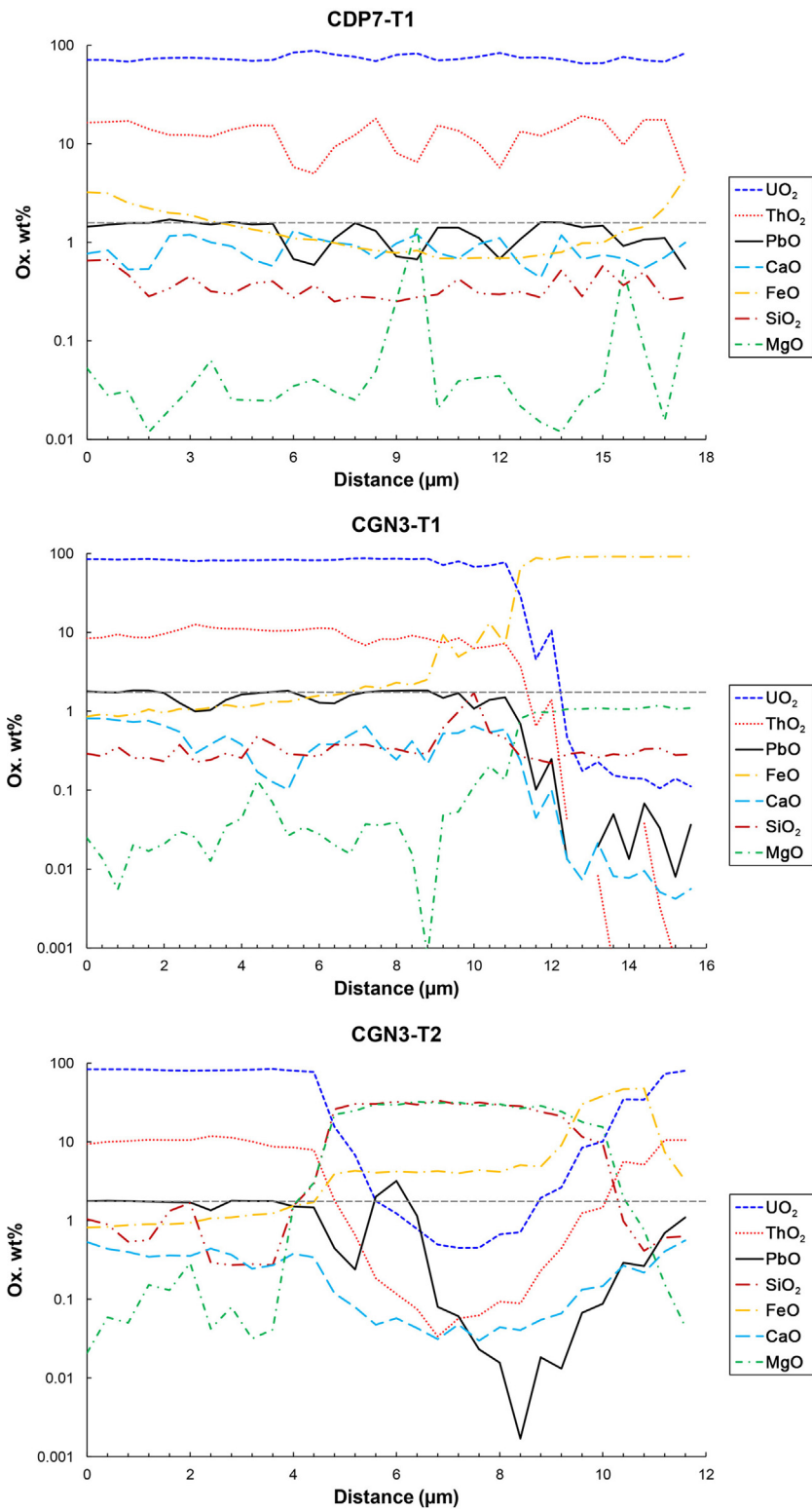


Fig. 7. Electron microprobe traverses across uraninite crystals (see Fig. 6 for their position). Horizontal dashed lines indicate PbO plateau.

400 °C. In troctolites, diopside breakdown is accompanied by an increase in the modal amount of tremolite (and fayalite at 300 °C). In serpentinized harzburgites, diopside reacts at 300 °C with brucite and magnetite to form andradite and antigorite (cf. reaction n. 44 in Frost and Beard, 2007; Fig. 12a, c). Talc becomes abundant in pegmatoid serpentinites at 400 °C, but at 300 °C it only forms when the rocks react with Fe-gabbro derived fluid.

Formation of talc is enhanced by the low pH, high Si and low Ca activities of the Fe-gabbro-reacted hydrothermal fluid. At high *W/R ratios*, in both fresh and serpentinized dunites and harzburgites, brucite reacts with either the harzburgite-reacted fluid or the Fe-gabbro reacted fluid to form antigorite or clinocllore, respectively. Talc is formed in Si-rich systems, i.e., those involving Si-rich lithologies (troctolites, pegmatoid serpentinite) or fluids

Table 6
Trace element composition of magnetite (LA-ICP-MS).

Location Sample Rock Type	Site 1 CO14 Mag-rich diopsidite n = 16			Site 1 LIC14 Nodular ore n = 16			Site 2 ECL1 Fine-grained disseminated ore n = 10			Site 2 CRY1 Vein ore n = 14			Site 3 LAR2A Mag-rich pegmatoid serpentinite n = 25			Site 3 CGN3 Di-rich nodular ore n = 13			
	DL (ppm) ± 2s	min	Max	Median	min	Max	Median	min	Max	Median	min	Max	Median	min	Max	Median	min	Max	Median
²⁴ Mg	11 ± 7	9357	11350	10216	21021	29568	24112	6149	7259	6696	7773	8481	8146	4173	8150	5629	5992	6945	6311
²⁸ Si	1020 ± 1895	<1020	1348	<1020	BDL			<1020	1572	<1020	BDL			<1020	2303	<1020	BDL		
⁴³ Ca	325 ± 93	BDL			BDL			BDL			BDL			BDL			BDL		
⁴⁷ Ti	6 ± 4	42	75	59	44	214	182	396	635	570	54	387	263	227	435	315	41	108	70
⁵¹ V	0.3 ± 0.2	13	43	23	5	81	29	7	30	17	<0.3	135	5	40	118	64	<0.3	33	6
⁵³ Cr	8 ± 3	BDL			BDL			<8	154	32	<8	14	<8	<8	64	<8	BDL		
⁵⁵ Mn	4 ± 1	3669	4246	4025	4318	5360	4991	2558	2706	2620	2903	3086	2984	2927	3394	3154	2797	3016	2940
⁵⁹ Co	0.3 ± 0.2	376	411	393	540	603	565	74	86	78	132	171	151	316	365	332	264	289	273
⁶⁰ Ni	8 ± 5	175	257	223	9	256	82	413	482	429	80	726	484	505	762	672	49	111	89
⁶⁶ Zn	2 ± 1	100	125	109	117	173	157	96	104	101	133	195	163	46	103	96	70	80	77
⁹⁸ Mo	0.5 ± 0.3	BDL			<0.5	1.3	<0.5	<0.5	0.2	<0.5	BDL			<0.5	1.3	<0.5	<0.5	1.8	1.1
⁹⁰ Zr	0.1 ± 0.1	BDL			<0.1	0.7	<0.1	0.1	0.6	0.3	nd			<0.1	2.1	0.1	<0.1	1.7	0.4
Co/Ni				1.8			6.9			0.2			0.3			0.5			3.1

s = sample standard deviation.

BDL = below detection limit.

nd = not determined.

(Fe-gabbro-reacted fluids). In the systems dominated by Fe-gabbro-reacted fluids, talc replaces forsterite and antigorite, thus forming talc + magnetite + clinocllore assemblages.

5. Discussion

5.1. Cogne as an ultramafic-hosted subseafloor hydrothermal deposit

5.1.1. Constraints from magnetite geochemistry and ocean seafloor studies

Important clues about the origin of the Cogne magnetite can be derived from the comparison with existing published datasets for magnetite from various genetic environments. The Cogne magnetite is poor in Ti and Cr (<640 ppm and <150 ppm, respectively), which is a typical feature for hydrothermal magnetite (Fig. 13). In fact, based on the data compiled by Dare et al. (2014), hydrothermal magnetite can be distinguished from magmatic magnetite, because the former has generally low Ti contents (<10,000 ppm) and high Ni/Cr ratios (≥ 1), in virtue of the higher mobility of Ni in aqueous fluids. Cogne magnetite is also poor in V (<140 ppm) and rich in Mn (>2500 ppm), similar to hydrothermal magnetite from skarn deposits (Fig. 14). However, the Cogne magnetite ore was not emplaced in carbonate rocks but in mantle serpentinites, as testified by the geochemical and textural features of the host rocks.

Serpentinization of peridotites can produce magnetite that is depleted in Cr, Ti, V and Ni compared to the primary magmatic magnetite (Boutroy et al., 2014). However, serpentinization alone cannot account for the amount of magnetite observed in most of Cogne rocks. In fact, magnetite production during serpentinization is limited by the amount of FeO available in the peridotite, which is commonly less than 10 wt% (Bodinier and Godard, 2003). Therefore, an efficient mechanism of mobilization and concentration of Fe is needed to explain the formation of the Cogne deposit.

Low-T (100–300 °C) hydrothermal fluids causing peridotite serpentinization at high W/R can leach Fe from the peridotite and precipitate it as magnetite in veins (up to a few cm-thick), as reported for the Bou Azzer ophiolite, Morocco (Gahlan et al., 2006). However, the compositions of Bou Azzer vein magnetites, although considerably depleted in trace elements as a consequence of their low formation temperatures (Nadoll and Koenig, 2011), are very differ-

ent from those of Cogne magnetites. The latter have higher Co/Ni ratios (0.2–67 vs. 0.004–0.12) and are richer in Mn (2600–5000 vs. 400–470 ppm), Zn (80–160 vs. 3–20 ppm) and Mg (5600–24000 vs. 97–1000 ppm). These differences suggest that the formation of Cogne magnetite took place under substantially dissimilar physicochemical conditions.

Some indications on the various factors that controlled the composition of Cogne magnetite can be derived from the PCA (Fig. 9). The PC1 clearly discriminates high-(Mg, Mn, Co, Zn) magnetites in nodular ores and diopsidites from high-(Ni, V, Ti) magnetites in fine-grained disseminated ore and in magnetite-rich pegmatoid serpentinite. The relatively low Mn, Co and Zn contents in the host rocks and the fluid-compatible nature of these metals suggests that the composition of the high-(Mg, Mn, Co, Zn) magnetites was controlled by an externally-buffered fluid (cf. Dare et al., 2014; Nadoll et al., 2014). The high Co/Ni ratios these magnetites (Table 6) also support this hypothesis, because it would suggest a mafic metal source (cf. Melekestseva et al., 2013), which is in contrast with the ultramafic nature of most of the Cogne host rocks. On the contrary, the high-(Ni, V, Ti) magnetites are more enriched in elements that are weakly mobile and/or relatively abundant in the host rocks, suggesting formation under rock-buffered conditions (cf. Nadoll et al., 2014). The PC1 may thus be interpreted as reflecting magnetite formation under different W/R ratios from possibly similar parent fluids. The PC2 further discriminates between the different host rocks (i.e., high-V magnetite in pegmatoid serpentinite and high-Ti magnetite in serpentinized mantle peridotites). Magnetite in veins shows intermediate geochemical features between hydrothermal fluid-buffered and host rock-affected compositions.

Hydrothermal fluids carrying a significant load of transition metals (high Fe, Mn, Cu, Zn ± Co ± Ni) issue from ultramafic substrates in high-T (>350 °C) hydrothermal systems associated with oceanic core complexes in slow-spreading mid-oceanic ridges, such as at Rainbow and Logatchev on the Mid-Atlantic Ridge (Douville et al., 2002; Andreani et al., 2014). In particular, the hydrothermal vent fluids at Rainbow are the richest in Co (Douville et al., 2002), have the highest Co/Ni ratios (~4) and are probably saturated in magnetite + chlorite + talc (Seyfried et al., 2011). The surveyed portion of the Rainbow hydrothermal deposit is almost entirely made up of sulphides (Fouquet et al., 2010; Marques et al., 2006, 2007), as expected for the upper part of a

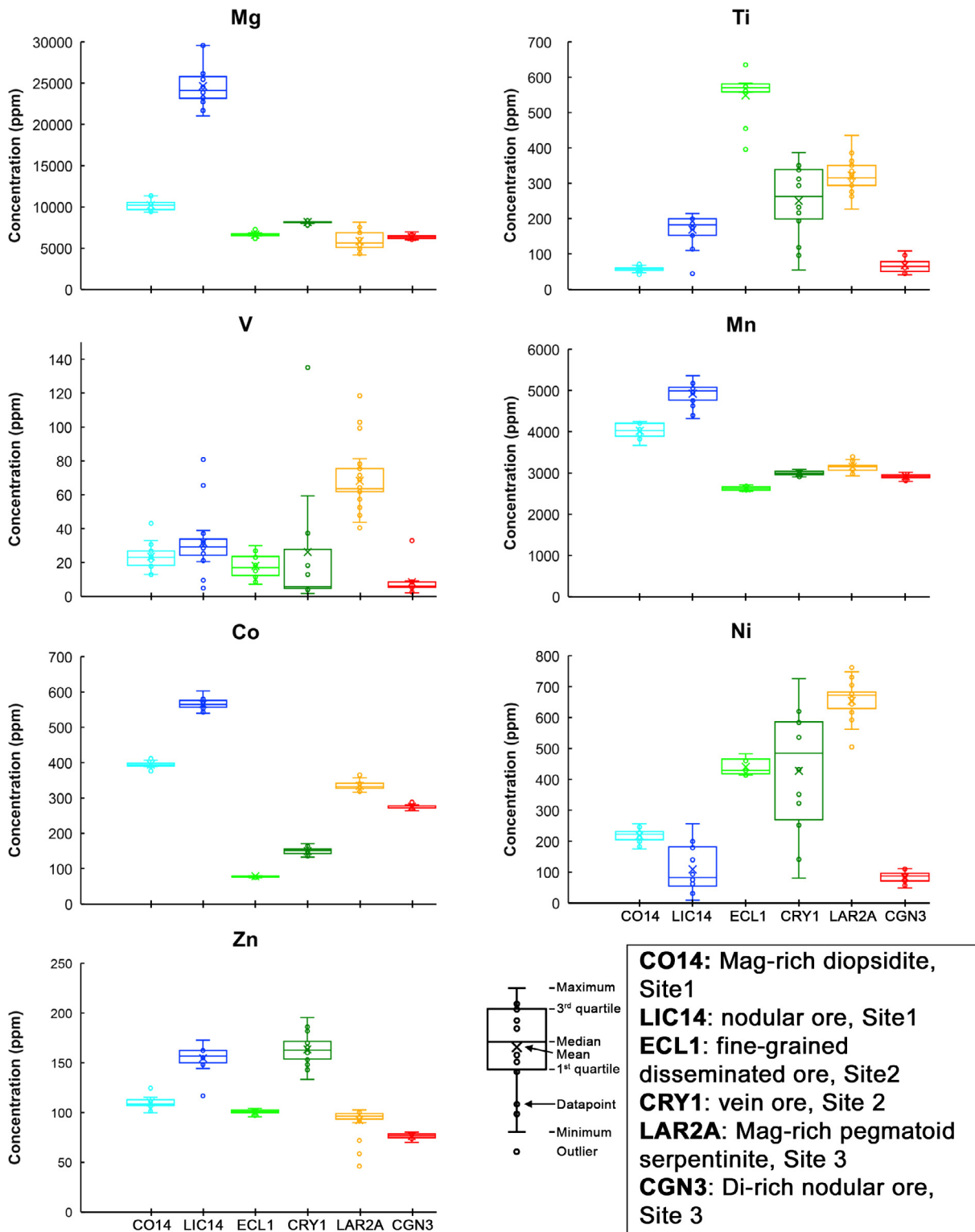


Fig. 8. Box and whiskers plot of magnetite trace element composition.

seafloor hydrothermal system, where the hot hydrothermal fluid mixes with seawater (Janecky and Seyfried, 1984). Notwithstanding this, at Rainbow, hydrothermal magnetite is locally abundant in serpentinites hosting sulphide stockworks and in semi-massive sulphides, where magnetite sometimes replaces pyrite (Marques, 2005). Magnetite forming coarse-grained disseminations in the serpentinites that host stockworks at Rainbow precip-

itated later than the sulphides during a distinct hydrothermal stage (Marques et al., 2006) and, notably, has a similar geochemical fingerprint as magnetite in fine-grained disseminations in serpentinized peridotites at Cogne (the concentrations of the trace elements, with the exception of Si, are in the same order of magnitude). Recently, Yildırım et al. (2016) described a hydrothermal magnetite mineralization in a non-metamorphic volcanogenic

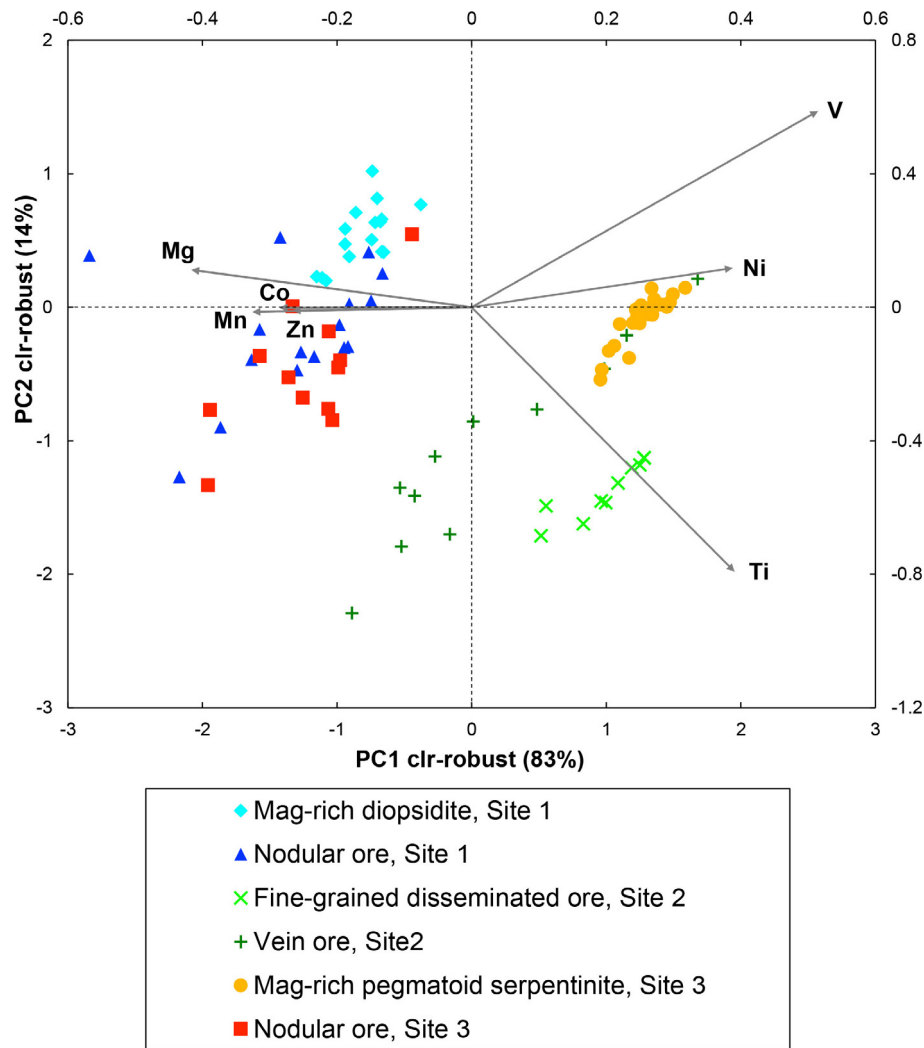


Fig. 9. Robust-PCA of magnetite trace element composition. Coordinates of datapoints (scores) are on left and lower horizontal axes. Coordinates of variables (loadings) are on right and upper horizontal axes.

massive-sulphide (VMS) deposit from the Upper Triassic–Upper Cretaceous Koçali complex, a Tethyan ophiolite in Turkey. These findings and the above observations support the possibility that Cogne magnetite has directly formed in a seafloor hydrothermal system. The presence of a positive magnetic anomaly at Rainbow has been ascribed to a $\sim 2 \cdot 10^6 \text{ m}^3$ magnetite-rich stockwork zone (Szitkar et al., 2014). If this volume was entirely composed of magnetite, it would correspond to 10 Mt of mineral, which is on the same order of magnitude as the estimated amount of magnetite at Cogne (~ 12 Mt). It is worth noting that the Rainbow hydrothermal system is still highly active (Fouquet et al., 2010) and its vent fluids are magnetite-saturated (Seyfried et al., 2011). It can thus be inferred that the Rainbow hydrothermal system may eventually produce at depth a magnetite deposit of comparable size as Cogne.

In such a scenario, the general scarcity of sulphides at Cogne, along with their presence in the veins above the main magnetite bodies, suggest that the exposed mineralized section represents the deep segment of a seafloor, ultramafic-hosted, high-temperature hydrothermal system, which was possibly associated with shallower, now eroded, sulphide-rich bodies. According to this interpretation, the magnetite + sulphide veins and fine-grained disseminations in the hanging wall serpentinite (Site 2) may mark the transition between the magnetite-rich and the sulphide-rich portions of the hydrothermal system (Fig. 15).

5.1.2. Geological, geochronological and textural constraints

The Cogne mantle peridotites underwent complete serpentinization at 200–300 °C beneath the seafloor of the Jurassic Piedmont-Liguria ocean (Carbonin et al., 2014). Our radiometric data on magnetite-associated uraninite (152.8 ± 1.3 Ma) places the ore-forming event in proximity of the Kimmeridgian-Tithonian boundary (152.1 ± 0.9 Ma). This age overlaps with that of the spreading of the Piedmont-Liguria ocean, as inferred by biochronological dating of supra-ophiolitic deep-sea sediments (radiolarites), whose oldest ages span from Late Bajocian to Middle Bathonian (~ 168 Ma; Cordey et al., 2012), and by radiometric dating of magmatic rocks, which places the latest magma pulses (mainly plagiogranites) in the Western Alps and Liguria in the Kimmeridgian-Tithonian ($\sim 157.3 \pm 1.0$ – ~ 145.5 Ma; Lombardo et al., 2002; Manatschal and Müntener, 2009 and references therein).

Very little information can be obtained about the original lithological and thermal structure of the oceanic lithosphere at Cogne, because of the limited exposure. Some indirect information can be obtained from the nearby Mt. Avic serpentinite massif (Fig. 1). Although located in a different structural position in the orogen (see Dal Piaz et al., 2010), the Mt. Avic massif provides the most complete section of the oceanic lithosphere of the Alpine Tethys in the southern Valle d'Aosta region. In the Mt. Avic massif,

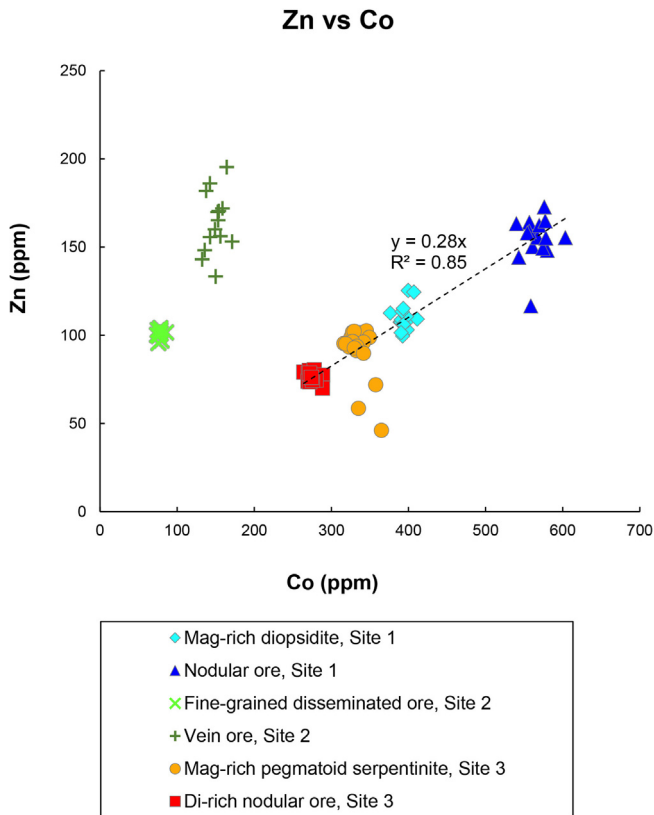


Fig. 10. Co vs. Ni relationships in magnetite. Regression line (dashed) for magnetite-rich samples from Site 1 and 3 shows linear relationship between Co and Ni.

dominant serpentinized mantle peridotites, associated with gabbroic intrusions (Mg-metagabbros), rodingitic dykes, minor Fe-Ti-oxide metagabbros and other metabasites (Dal Piaz et al., 2010; Fontana et al., 2008, 2015; Panseri et al., 2008), are thought to have been exposed on the seafloor in an oceanic core complex (Tartarotti et al., 2015). This is consistent with the proposed

slow- to ultra-slow nature of the Piedmont-Liguria ocean (Manatschal et al., 2011; Manatschal and Müntener, 2009; Piccardo, 2008). Jurassic magmatic activity in the Mt. Avic massif was sufficient to sustain high-temperature hydrothermal convection cells, as testified by widespread, small, massive sulphide (Cu-Fe-Zn) deposits, which are mostly associated with metabasites (Castello et al., 1980; Castello, 1981; Martin et al., 2008; Dal Piaz et al., 2010; Fantone et al., 2014) and are thought to have formed in the seafloor (Martin et al., 2008). The distinctive enrichment in Co and Cu observed in Cogne nodular and vein magnetite ores, respectively, as well as the low Ni content in all magnetite ore types, suggests a contribution from mafic sources or a combined contribution from ultramafic and mafic sources, as observed in some ultramafic-hosted, mid-ocean ridge, hydrothermal deposits (e.g., Rainbow, Fouquet et al., 2010; Marques et al., 2006; Semenov, Melekestseva et al., 2014) and in other ultramafic-hosted VMS deposits in ophiolitic belts (Melekestseva et al., 2013). In analogy with these modern and ancient examples, also at Cogne the presence of deep magmatic intrusions (gabbro) would be required to provide heat and suitable chemical conditions (low pH) to produce metal-rich fluids (e.g., Marques et al., 2006; Seyfried et al., 2011). Gabbroic intrusions, mainly represented by gabbros and Fe-Ti gabbros, are not observed in the small Cogne unit, but are common in the wider Mt. Avic area (see above) and in the other ophiolitic units in southern Valle d'Aosta (Grivola-Urtier and Zermatt-Saas units; Benciolini et al., 1988; Bocchio et al., 2000; Dal Piaz et al., 2010; Polino et al., 2014). Therefore, we infer that similar rock types could have occurred also at Cogne in the original oceanic lithosphere section.

The texture, geochemistry (low Co/Ni, high Cr) and relict mineralogy (bastites, Mg-Al-rich chromite) of Site 2 magnetite-enriched serpentinites suggest that the host rock was a mantle harzburgite, with composition comparable with that of modern abyssal peridotites. However, chemical and textural evidence from both Site 1 and Site 3 indicates that part of the hydrothermal ore was emplaced in more atypical serpentinites, which exhibit a ghost pegmatoid texture marked by interlobate domains separated by coronae structures (Fig. 3f). Similar textures have been described in some troctolites from modern oceanic and ancient ophiolitic settings (Blackman et al., 2006; Renna and Tribuzio, 2011). These rocks

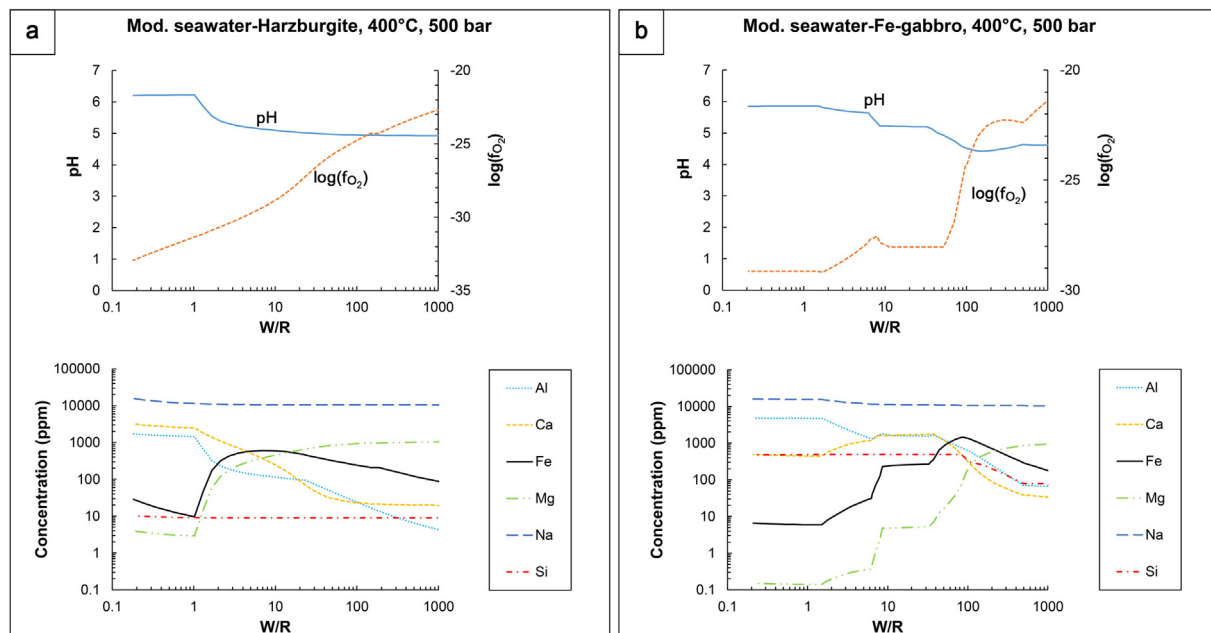


Fig. 11. Variation in pH, f_{O_2} and element concentrations in modified seawater equilibrated with harzburgite (a) or Fe-gabbro (b) at 400 °C at various W/R.

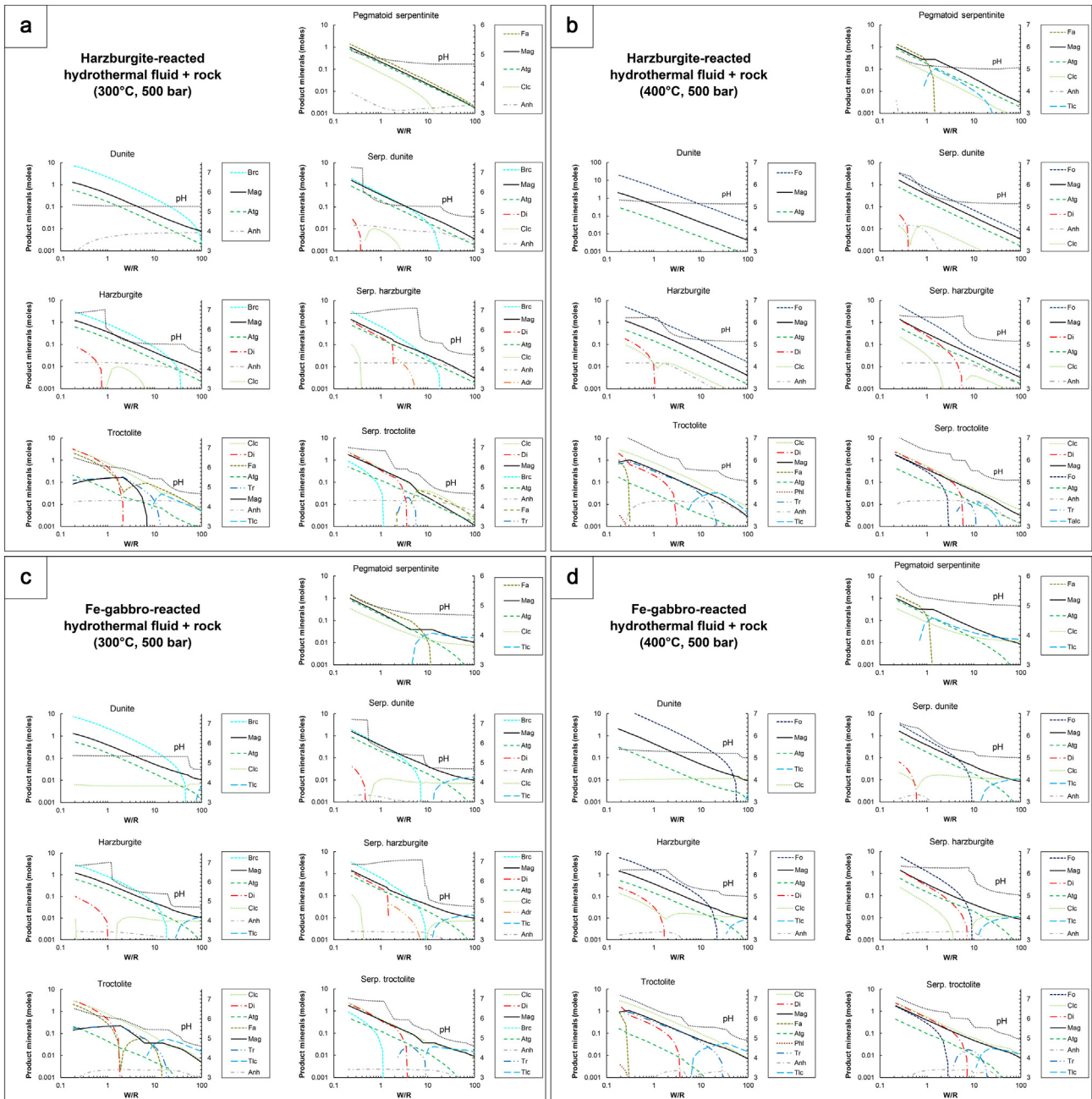


Fig. 12. Mineral assemblages and variation in pH produced by reaction of model hydrothermal fluids with selected rock types. Harzburgite-reacted fluid reacting with rocks at a) 300 °C and 500 bar b) 400 °C and 500 bar. Fe-gabbro-reacted fluid reacting with rocks at c) 300 °C and 500 bar d) 400 °C and 500 bar.

are interpreted to have formed from melt-impregnation and melt-peridotite reactions, which dissolved orthopyroxene and partially dissolved olivine producing rounded or embayed grain boundaries (Drouin et al., 2009; Renna and Tribuzio, 2011; Suhr et al., 2008). In particular, olivine-rich troctolites originating from melt-peridotite reactions are usually coarse-grained and can show a harrisitic texture (Renna and Tribuzio, 2011), which is reminiscent of the “harrisitic” texture of some nodular ores at Cogné. This suggests that many, if not most, nodular ores at Cogné formed by hydrothermal alteration of original serpentinitized troctolites, with magnetite preferentially replacing the original olivine domains.

5.1.3. Insights from thermodynamic modelling

From a qualitative point of view, interaction of various types of fresh or serpentinitized mantle rocks with either a harzburgite-

reacted fluid at intermediate to high W/R or a Fe-gabbro-reacted hydrothermal fluid at intermediate W/R (Fig. 12) can produce mineral assemblages made of magnetite + antigorite + clinocllore ± b-cucite (at 300 °C) ± forsterite (at 400 °C), which resemble the most common mineral assemblages in the Cogné magnetite ores. However, even when the natural mineral assemblage is qualitatively reproduced, the calculated modal magnetite content invariably remains too low to produce a magnetite ore. This indicates that our model fluids are not sufficiently Fe-rich to account for the formation of the Cogné deposit. Note that a Rainbow-type fluid (Table 7) would produce broadly similar mineral assemblages as our model fluids, since its Na, Mg, Si, Fe, Cl concentrations are fairly similar. We could not envisage any other reasonable substrate lithology which could have released significantly higher Fe to the hydrothermal fluids under reasonable conditions. This suggests

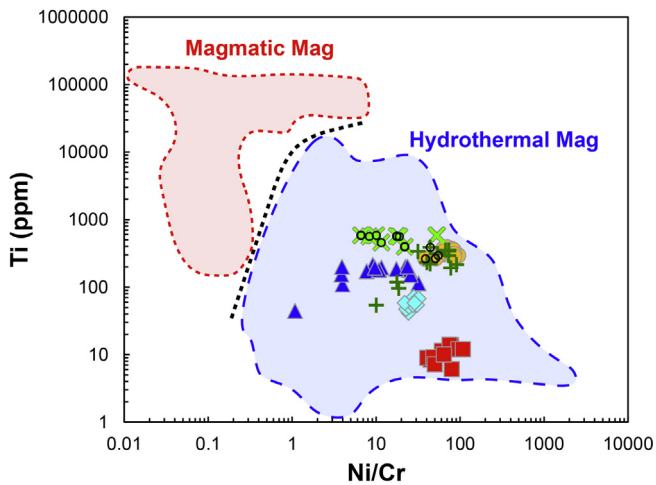


Fig. 13. Compositions of Cogne magnetites plotted in the discrimination diagram by Dare et al. (2014). Magnetites with Cr contents above detection limit are circled. The other data points are plotted assuming a Cr value equal to the detection limit of 8 ppm. Although this may have unduly shifted the points to lower Ni/Cr ratios, the strong hydrothermal character of the Cogne magnetites remains evident.

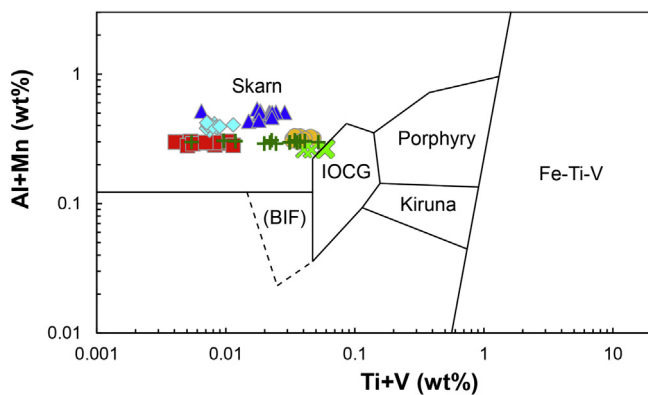


Fig. 14. Compositions of Cogne magnetites in the discrimination diagram of Dupuis and Beaudoin, 2011. LA-ICP-MS data are not available for Al (generally $\ll 0.1$ wt% based on EPMA data), therefore the plotted (Mn + Al) contents should be considered as minimum values.

that additional processes other than simple seawater/rock reactions have played a role in the formation of the magnetite parent fluids.

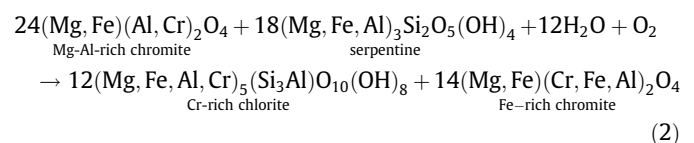
One such process could be phase separation in the hydrothermal fluid, which could have produced brines enriched in weakly volatile Fe. Phase separation is commonly invoked to explain the wide chlorinity range observed in modern seafloor hydrothermal vent fluids (e.g., Bischoff and Rosenbauer, 1987; Charlou et al., 2002; Douville et al., 2002; Foustoukos and Seyfried, 2007; Pester et al., 2014; Seyfried et al., 2011). A higher chlorinity would enhance solubility of metals as chloride complexes. At the same time, H_2S partitioning into the vapour phase would cause sulphide undersaturation in the brine (Bischoff and Rosenbauer, 1987; Fouquet et al., 2010; Seyfried et al., 2004, 2010; Von Damm, 2004), thus delaying sulphide precipitation. This is in agreement with the general scarcity of sulphides in the Cogne magnetite ores. The presence of chalcophile metals in the fluid is still testified by Cu sulphides in magnetite veins from Site 2. In this case, the transition from bornite + magnetite to chalcopyrite + magnetite assemblages suggests a progressive variation in the parent fluids towards higher H_2S activity or lower Cu/Fe ratios (cf. Seyfried et al., 2004, 2010).

Another process which could potentially lead to enhanced Fe concentrations in the fluid is the incorporation of a magmatic gaseous component, which could promote acidification and thus increase Fe solubility (cf. Berkenbosch et al., 2012; de Ronde et al., 2011). However, assuming a gas composition similar to that of gases emitted from mafic lavas (Erta 'Ale volcano, Ethiopia; Sawyer et al., 2008), it can be calculated that a relatively high condensed gas/fluid mass ratio of 1:10 would increase the Fe concentrations only by a factor of ~ 2.3 . This increase is too small to allow a significant increase in the final amount of precipitated magnetite. Therefore, phase separation remains the most likely hypothesis.

Another feature that is not explained by our models is the diopside-rich gangue observed at Site 3. Textural relationships suggest that diopside formed during a late stage of magnetite mineralization, most likely from a fluid with higher pH and/or higher Ca^{2+} activity (see Fig. 9 in Bach and Klein, 2009). This fluid could have derived from serpentinization of country peridotites and troctolites, and may thus have some affinity with rodingite-forming fluids. Alternatively, a higher Ca content could result from more extensive interaction with gabbroic rocks. The possible role of gabbroic rocks in producing Ca-Si-(Al)-rich fluids has been suggested, for instance, for fluids responsible for strong calcic metasomatism in fault zones in modern oceanic core complexes (Boschi et al., 2006).

5.2. Alternative hypotheses

As ultramafic rocks in ophiolitic massifs often contain accumulations of chromite (e.g., Bédard and Hébert, 1998), a potential origin of magnetite in Sites 1 and 3 could be by leaching of Cr from former chromitite bodies. Indeed, Cr appears to be mobile during high-temperature (>500 – 550 °C) peridotite-water interactions, as shown by Arai and Akizawa (2014) for the Oman ophiolite. Also, in the Mt. Avic massif, some small-scale magnetite ores were apparently formed after former chromitites (Diella et al., 1994; Rossetti et al., 2009). There are two lines of evidence against this hypothesis for the Cogne magnetite. First, in the Mt. Avic ores, chromite is still preserved in the cores of the magnetite grains (Diella et al., 1994; Fontana et al., 2008; Rossetti et al., 2009), whereas neither chromite relicts nor Cr-rich magnetite cores are found in nodular and vein ores at Cogne. Second, there is no evidence for a high-temperature alteration at Cogne such as that described in the Oman ophiolite by Arai and Akizawa (2014). At the temperatures under which serpentinization and successive hydrothermal metasomatism at Cogne took place (200–300 °C and 300–400 °C, respectively; Carbonin et al., 2014), Cr is essentially immobile and any Cr dissolved at higher temperatures deeper in the system should be precipitated (Arai and Akizawa, 2014). The immobility of Cr during magnetite mineralization is testified by the mantle peridotites containing the fine-grained disseminated magnetite from Site 2, which have similar bulk-rock Cr content as their magnetite-poor counterparts (Fig. 5). In these rocks, the original Mg-Al-rich chromite (the main Cr carrier) was replaced with *no Cr loss* by Fe-rich chromite + Cr-rich chlorite, according to reactions of the type



(cf. Mellini et al., 2005; Merlini et al., 2009), and then overgrown by Cr-poor magnetite (Fig. 4d). The P-T conditions for the subsequent Alpine metamorphism at Cogne are not precisely known. However, assuming a typical subduction geothermal gradient (<10 °C/km), the coexistence of lizardite and antigorite in both

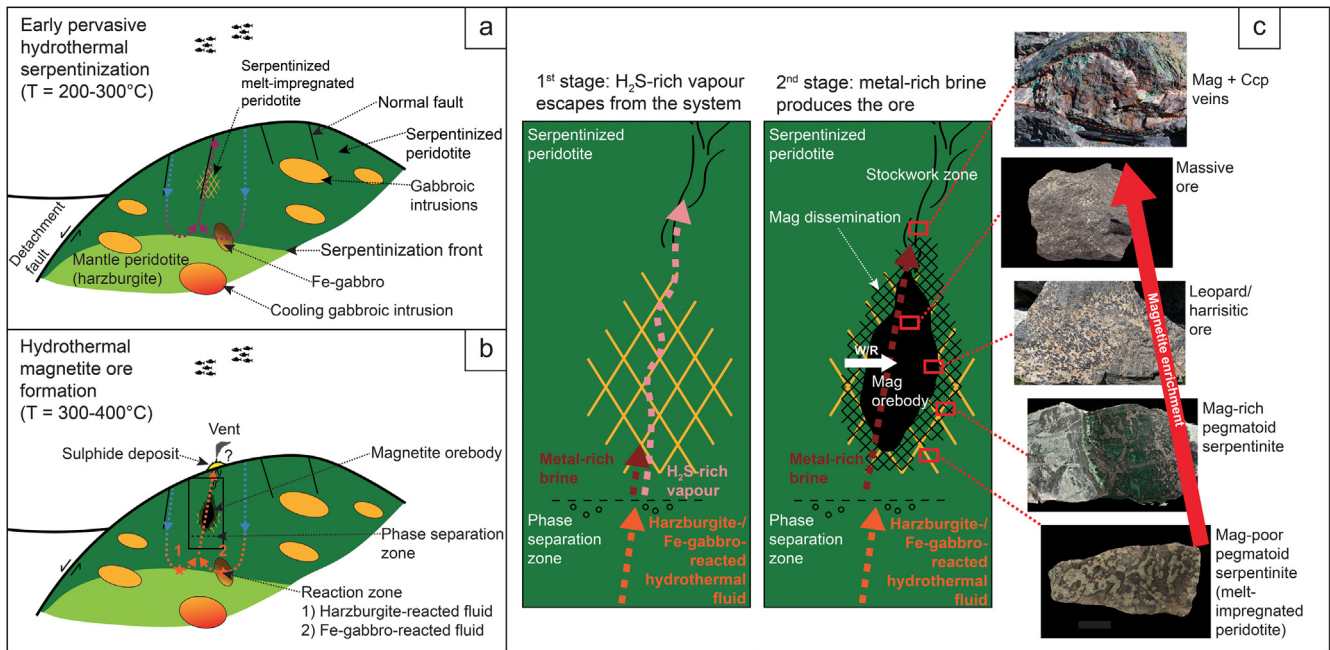


Fig. 15. Interpreted schematic evolution of the Cogne deposit. a) Formation of an oceanic core complex made up of mantle peridotites intruded by gabbros and Fe-gabbros, and locally impregnated by melts. Early circulation of hydrothermal fluids produces extensive serpentinization at relatively low-T (lizardite stability field). High water/rock ratios are possibly attained thanks to fluid focussing along fractures and faults. b) Convective circulation of seawater produces high-T hydrothermal fluids that leach metals from harzburgites and Fe-gabbros. These fluids undergo phase separation and produce a magnetite-rich body at depth and a sulphide mound on the seafloor. A magnetite-sulphide stockwork zone marks the transition between the magnetite orebody and the sulphide mound. c) Close-up of the framed region in b). Phase separation produces an H_2S -rich vapour that quickly escapes from the system and a dense metal-rich brine. Then, the upwelling brine reacts with the serpentinites at various fluid/rock ratios and precipitates magnetite, producing fine-grained disseminated, nodular and replacive massive ores. Further upwelling of the magnetite-saturated fluids along fractures produces magnetite + chalcopyrite veins (stockwork zone) and fine-grained disseminations in shallower serpentinites.

Table 7

Composition of model hydrothermal fluids and the Rainbow vent fluid (mmol/kg solution).

	Harzburgite-reacted	Fe-gabbro-reacted	Rainbow
Na	460.2	464.4	570.0
Ca	9.2	12.0	67.7
Mg	15.6	3.1	1.7
Si	0.3	17.5	7.3
Fe	10.8	25.8	22.2
Al	4.7	27.6	0.0029
Cl ⁻	535.4	527.3	757.0

serpentinized peridotites and pegmatoid serpentinites suggests temperatures not exceeding 390 °C (Schwartz et al., 2013), which are too low to determine significant mobilization of Cr.

Iron (Mn) oxyhydroxides and Fe sulphide deposits are the most common forms of Fe accumulation in modern seafloor hydrothermal settings (e.g., Rona, 1988). In principle, magnetite may form by reduction and dehydration of Fe-oxyhydroxides or by desulphurization of Fe-sulphides during metamorphism. However, our geochronological data demonstrate that the magnetite-forming event was coeval with the spreading of the Piedmont-Liguria ocean and thus predates Alpine metamorphism. Also the geochemistry of Cogne magnetite ores and associated rocks contradicts the metamorphic hypothesis. In fact, in Fe-oxyhydroxide accumulations, an enrichment in trace elements such as P and Sr is typically observed (e.g., Hekinian et al., 1993; Puteanus et al., 1991). A similar enrichment is indeed preserved in seafloor hydrothermal Mn-(Fe) deposits in southern Valle d'Aosta ophiolites (median $P_2O_5 = 0.06$ wt%, median Sr = 1650 ppm; Tumiti et al., 2010), which were metamorphosed up to eclogite-facies conditions ($T = 550 \pm 60$ °C, $P = 2.1 \pm 0.3$ GPa; Martin et al., 2008; Tumiti et al., 2015), but it is not observed in Cogne ores ($P_2O_5 \leq 0.01$ wt%, median Sr = 1.6 ppm). In the same ophiolites, sulphide (pyrite +

chalcopyrite) deposits show no evidence of S mobilization and depletion linked to subduction metamorphism (Giacometti et al., 2014). Consistently, serpentinized mantle peridotites overlying the Cogne magnetite orebody are not depleted in S (Table 4).

5.3. The role of the Alpine event

The present structural position of the Cogne serpentinite, the lithological associations and the shape of the orebodies are in part the result of the tectonic activity that accompanied the Alpine orogenesis. The main magnetite orebodies at Site 1 and Site 3 behaved as rigid masses during the early ductile deformation events and they were affected by only low degrees of shear deformation, thus preserving the original textures and the proportions between magnetite and gangue minerals. The Alpine deformation was more intense at Site 2, which was probably located in a peripheral position with respect to the main orebody, where the fine-grained disseminated ores and the associated veins were dismembered into lenses. The Alpine metamorphism did not promote significant magnetite remobilization, as testified by the lack of isotopic resetting in uraninite inclusions in magnetite. The Alpine metamorphism is possibly responsible for the transformation of lizardite into antigorite, which is observed also in rocks that do not contain hydrothermal mineralization (i.e., magnetite-poor serpentinized peridotites and pegmatoid serpentinites). In any case the metamorphic temperatures were not sufficient to cause significant serpentine dehydration, since neoblastic forsterite is not widespread and is only found within the nodular ore at Site 1. The restriction of neoblastic forsterite to this specific site suggests that its formation could be related to higher temperature conditions (~400 °C) being attained locally during the magnetite hydrothermal event, rather than to the subsequent metamorphism. Based on the above considerations, we conclude that Alpine metamorphism did not

play a significant role in concentrating magnetite, although Alpine deformation may have pulled away portions of the deposit (now exposed at sites 1, 2 and 3) that could have been much closer to one another in their original oceanic setting.

5.4. Stages of formation of the Cogne deposit

Considering all available data, we propose the following sequence of events for the formation of the Cogne deposit (Fig. 15):

- 1) Formation of an oceanic core complex made of mantle peridotites, containing bodies of gabbros and Cr-poor melt-impregnated peridotites (troctolites).
- 2) Extensive low-temperature serpentinization, producing lizardite serpentinites containing a first generation of disseminated magnetite (Cr-bearing in mantle peridotites and Cr-free in melt impregnated peridotites). This process probably occurred at high water/rock ratios and determined the complete serpentinization of the primary silicates and an extensive loss of Ca.
- 3) Production of a high-temperature, Fe-rich hydrothermal fluid by reaction of downwelling seawater with substrate rocks. The involvement of Fe-gabbros in the reaction zone is likely, as this would enhance the content of Fe in the fluid.
- 4) Phase separation in the upwelling hydrothermal fluid, producing a more Fe-rich brine.
- 5) Reaction of the upwelling hot brine (~300–400 °C) with various lithologies (serpentinites after mantle peridotites and troctolites) at various fluid/rock ratios, producing the dissolution of lizardite and the precipitation of abundant magnetite along with antigorite and clinocllore (±brucite and forsterite), forming fine-grained disseminated, nodular and massive replacive ores. Further upwelling of the magnetite-buffered fluid produced magnetite + Cu-sulphide + antigorite veins and fine-grained disseminations in shallower serpentinites.
- 6) Circulation of late fluids with higher pH and/or higher Ca²⁺ activity, producing diopside-rich, magnetite-bearing metasomatic rocks.

6. Conclusions

The Cogne magnetite deposit was formed at ~150 Ma by hydrothermal processes during an advanced stage of the opening of the Piedmont–Liguria ocean. Based on geological and petrographic features and on geochemical and mineralogical similarities with some modern ultramafic-hosted VMS deposits on mid-ocean ridges, the exposed mineralized section at Cogne may represent the deep segment of a seafloor, high-temperature (~300–400 °C) hydrothermal system, which was possibly associated with shallower, now eroded, sulphide-rich bodies (Fig. 15). As suggested by thermodynamic modelling, simple seawater-rock interactions cannot produce the Fe endowment observed at Cogne. Fractionation processes such as phase separation were probably critical to generate sufficiently Fe-rich hydrothermal fluids capable to precipitate large amounts of magnetite in various types of mantle host-rocks. The possible occurrence of similar ultramafic-hosted magnetite deposits in present-day oceanic settings could contribute to explain the presence of significant magnetic anomalies centred on active and inactive ultramafic-hosted hydrothermal fields (Fujii et al., 2016; Sztikar et al., 2014; Tivey and Dymont, 2010).

Acknowledgements

We thank Raul Carampin (CNR, IGG, Padua) and Andrea Risplendente (Earth Sciences Department, University of Milan) for

the technical assistance with the electron microprobe analyses. We are also grateful to Drs. Andreas Klügel and Patrick Monien (“Petrology of the Ocean Crust” research group, University of Bremen, Germany) for providing scientific and technical support during LA-ICP-MS measurements. We thank “Assessorato Territorio e Ambiente” of the Valle d’Aosta region for providing access to the archives of the Cogne mine. We are grateful to Patrick Nadoll and Paola Tartarotti for their constructive reviews and suggestions. This work was carried out during LT’s PhD at the University of Padua. PN acknowledges financial support by Progetto di Ateneo 2013 CPDA138741 “Copper metallogenesis and provenancing in the Alpine realm” (University of Padua).

Appendix A. Supplementary data

Supplementary data associated with this article can be found, in the online version, at <http://dx.doi.org/10.1016/j.oregeorev.2016.11.030>.

References

- Alexandre, P., Kyser, T.K., 2005. Effects of cationic substitutions and alteration in uraninite, and implications for the dating of uranium deposits. *Can. Mineral.* 43, 1005–1017.
- Andreani, M., Escartin, J., Delacour, A., Ildefonse, B., Godard, M., Dymont, J., Fallick, A. E., Fouquet, Y., 2014. Tectonic structure, lithology, and hydrothermal signature of the Rainbow massif (Mid-Atlantic Ridge 36° 14' N). *Geochem. Geophys. Geosyst.* 15, 3543–3571.
- Arai, S., Akizawa, N., 2014. Precipitation and dissolution of chromite by hydrothermal solutions in the Oman ophiolite: new behavior of Cr and chromite. *Am. Mineral.* 99, 28–34.
- Bach, W., Klein, F., 2009. The petrology of seafloor rodingites: insights from geochemical reaction path modeling. *Lithos* 112, 103–117.
- Bédard, J.H., Hébert, R., 1998. Formation of chromitites by assimilation of crustal pyroxenites and gabbros into peridotitic intrusions: North Arm Mountain massif, Bay of Islands ophiolite, Newfoundland, Canada. *J. Geophys. Res.-Sol. Ea.* 103, 5165–5184.
- Benciolini, L., Lombardo, B., Martin, S., 1988. Mineral chemistry and Fe/Mg exchange geothermometry of ferrogabbro-derived eclogites from the Northwestern Alps. *Neues. Jb. Miner. Abh.* 159, 199–222.
- Berkenbosch, H.A., de Ronde, C.E.J., Gemmel, J.B., McNeil, A.W., Goemann, K., 2012. Mineralogy and formation of black smoker chimneys from Brothers submarine volcano, Kermadec Arc. *Econ. Geol.* 107, 1613–1633.
- Berndt, M.E., Seyfried, W.E., Janecky, D.R., 1989. Plagioclase and epidote buffering of cation ratios in mid-ocean ridge hydrothermal fluids: experimental results in and near the supercritical region. *Geochim. Cosmochim. Acta* 53, 2283–2300.
- Bischoff, J.L., Rosenbauer, R.J., 1987. Phase separation in seafloor geothermal systems; an experimental study of the effects on metal transport. *Am. J. Sci.* 287, 953–978.
- Blackman, D.K., Ildefonse, B., John, B.E., Ohara, Y., Miller, D.J., MacLeod, C.J., Expedition 304/305 Scientists, 2006. Proceedings of the Integrated Ocean Drilling Program, vols. 304/305. Integrated Ocean Drilling Program Management International Inc, College Station, Texas.
- Bocchio, R., Benciolini, L., Martin, S., Tartarotti, P., 2000. Geochemistry of eclogitised Fe-Ti gabbros from various lithological settings (Aosta Valley ophiolites, Italian western Alps). *Protolith composition and eclogitic paragenesis. Period. Mineral.* 69, 217–237.
- Bodinier, J.-L., Godard, M., 2003. Orogenic, ophiolitic, and abyssal peridotites. In: Turekian, K.K., Holland, H.D. (Eds.), *The Mantle and Core: Treatise on Geochemistry*, second Ed. Elsevier, Oxford, pp. 103–167.
- Boschi, C., Früh-Green, G.L., Delacour, A., Karson, J.A., Kelley, D.S., 2006. Mass transfer and fluid flow during detachment faulting and development of an oceanic core complex, Atlantis Massif (MAR 30°N). *Geochem. Geophys. Geosyst.* 7.
- Boutroy, E., Dare, S.A., Beaudoin, G., Barnes, S.J., Lightfoot, P.C., 2014. Magnetite composition in Ni-Cu-PGE deposits worldwide: application to mineral exploration. *J. Geochem. Explor.* 145, 64–81.
- Bowles, J.F.W., 1990. Age dating of individual grains of uraninite in rocks from electron microprobe analyses. *Chem. Geol.* 83, 47–53.
- Bowles, J.F., 2015. Age dating from electron microprobe analyses of U, Th, and Pb: geological advantages and analytical difficulties. *Microsc. Microanal.* 21, 1114–1122.
- Carbonin, S., Martin, S., Tumati, S., Rossetti, P., 2014. Magnetite from the Cogne serpentinites (Piedmont ophiolite nappe, Italy). Insights into seafloor fluid–rock interaction. *Eur. J. Mineral.* 27, 31–50.
- Castello, P., Dal Piaz, G.V., Gosso, G., Kienast, J.R., Martin, S., Natale, P., Nervo, R., Polino, R., Venturelli, G., 1980. The Piedmont ophiolite nappe in the Aosta Valley and related ore deposits. In: Gruppo di Lavoro sulle Ophioliti Mediterranee. VI ophiolite field conference, Firenze. Field excursion book, pp. 171–192.

- Castello, P., 1981. Inventario delle mineralizzazioni a magnetite, ferro-rame e manganese del complesso piemontese dei calcescisti con pietre verdi in Valle d'Aosta. *Ofioliti* 6, 5–46.
- Charlou, J.L., Donval, J.P., Fouquet, Y., Jean-Baptiste, P., Holm, N., 2002. Geochemistry of high H₂ and CH₄ vent fluids issuing from ultramafic rocks at the Rainbow hydrothermal field (36°14'N, MAR). *Chem. Geol.* 191, 345–359.
- Cocherie, A., Albarede, F., 2001. An improved U-Th-Pb age calculation for electron microprobe dating of monazite. *Geochim. Cosmochim. Acta* 65, 4509–4522.
- Compagnoni, R., Elter, G., Fiora, L., Natale, P., Zucchetti, S., 1979. Nuove osservazioni sul giacimento di magnetite di Cogne in Valle d'Aosta. *Rend. Soc. Mineral. Petrol.* 35, 755–766.
- Compagnoni, R., Elter, G., Fiora, L., Natale, P., Zucchetti, S., 1981. Magnetite deposits in serpentinized lherzolites from the ophiolitic belt of the Western Alps, with special reference to the Cogne deposit (Aosta Valley). In: *Proceedings of the Intern. Symp. Mafic and Ultramafic Complexes*, Athens, pp. 376–394.
- Cordey, F., Tricart, P., Guillot, S., Schwartz, S., 2012. Dating the Tethyan Ocean in the Western Alps with radiolarite pebbles from synorogenic Oligocene molasse basins (southeast France). *Swiss J. Geosci.* 105, 39–48.
- Cross, A., Jaireth, S., Rapp, R., Armstrong, R., 2011. Reconnaissance-style EPMA chemical U-Th-Pb dating of uraninite. *Aust. J. Earth Sci.* 58, 675–683.
- Dal Piaz, G., Cortiana, G., Del Moro, A., Martin, S., Pennacchioni, G., Tartarotti, P., 2001. Tertiary age and paleostructural inferences of the eclogitic imprint in the Austroalpine outliers and Zermatt-Saas ophiolite, western Alps. *Int. J. Earth Sci.* 90, 668–684.
- Dal Piaz, G.V., Bistacchi, A., Massironi, M., 2003. Geological outline of the Alps. *Episodes* 26, 175–180.
- Dal Piaz, G.V., Gianotti, F., Monopoli, B., Pennacchioni, G., Tartarotti, P., Schiavo, A., 2010. Note illustrative della carta geologica d'Italia alla scala 1:50.000 Chatillon F. 91. *Ispra-Servizio Geologico d'Italia*, Treviso.
- Dare, S.A., Barnes, S.J., Beaudoin, G., Méric, J., Boutroy, E., Potvin-Doucet, C., 2014. Trace elements in magnetite as petrogenetic indicators. *Miner. Deposita* 49, 785–796.
- Debret, B., Andreani, M., Muñoz, M., Bolfan-Casanova, N., Carlut, J., Nicollet, C., Schwartz, S., Trcera, N., 2014. Evolution of Fe redox state in serpentine during subduction. *Earth Planet. Sci. Lett.* 400, 206–218.
- De Giusti, F., Dal Piaz, G.V., Massironi, M., Schiavo, A., 2003. Carta geotettonica della Valle d'Aosta. *Mem. Sci. Geol.* 55, 129–149.
- Della Giusta, A., Carbonin, S., Russo, U., 2011. Chromite to magnetite transformation: compositional variations and cation distributions (southern Aosta Valley, Western Alps, Italy). *Period. Mineral.* 80, 1–17.
- de Ronde, C.E.J., Massoth, G.J., Butterfield, D.A., Christenson, B.W., Ishibashi, J., Ditchburn, R.G., Hannington, M.D., Brathwaite, R.L., Lupton, J.E., Kamenetsky, V. S., Graham, I.J., Zellmer, G.F., Dziak, R.P., Embley, R.W., Dekov, V.M., Munnik, F., Lahr, J., Evans, L.J., Takai, K., 2011. Submarine hydrothermal activity and gold-rich mineralization at Brothers Volcano, Kermadec Arc, New Zealand. *Miner. Deposita* 46, 541–584.
- Di Colbataldo, D., Di Furia, E., Rossi, F., 1967. Il giacimento a magnetite di Cogne in Val d'Aosta. *Istituto Lombardo A101*, 361–394.
- Diella, V., Ferrario, A., Rossetti, P., 1994. The magnetite ore deposits of the southern Aosta Valley: chromitite transformed during an Alpine metamorphic event. *Ofioliti* 19, 247–256.
- Ding, K., Seyfried, W.E., 1992. Determination of Fe-Cl complexing in the low pressure supercritical region (NaCl fluid): iron solubility constraints on pH of seafloor hydrothermal fluids. *Geochim. Cosmochim. Acta* 56, 3681–3692.
- Douville, E., Charlou, J.L., Oelkers, E.H., Bienvenu, P., Colon, C.J., Donval, J.P., Fouquet, Y., Prieur, D., Appriou, P., 2002. The rainbow vent fluids (36°14' N, MAR): the influence of ultramafic rocks and phase separation on trace metal content in Mid-Atlantic Ridge hydrothermal fluids. *Chem. Geol.* 184, 37–48.
- Drouin, M., Godard, M., Ildefonse, B., Bruguier, O., Garrido, C.J., 2009. Geochemical and petrographic evidence for magmatic impregnation in the oceanic lithosphere at Atlantis Massif, Mid-Atlantic Ridge (IODP Hole U1309D, 30 N). *Chem. Geol.* 264, 71–88.
- Dupuis, C., Beaudoin, G., 2011. Discriminant diagrams for iron oxide trace element fingerprinting of mineral deposit types. *Miner. Deposita* 46, 319–335.
- Edmonds, H., 2010. Chemical signatures from hydrothermal venting on slow spreading ridges. In: Rona, P.A., Devey, C.W., Dymont, J., Murton, B.J. (Eds.), *Diversity of Hydrothermal Systems on Slow Spreading Ocean Ridges*. American Geophysical Union, Washington, DC, pp. 27–42.
- Elter, G., 1971. Schistes lustrés et ophiolites de la zone piémontaise entre Orco et Doire Baltée (Alpes Graies). *Hypothèses sur l'origine des ophiolites*. *Géologie Alpine* 47, 147–169.
- Evans, B.W., 2004. The serpentinite multisystem revisited: chrysotile is metastable. *Int. Geol. Rev.* 46, 479–506.
- Evans, B.W., 2010. Lizardite versus antigorite serpentinite: magnetite, hydrogen, and life (?). *Geology* 38, 879–882.
- Fantone, I., Grieco, G., Strini, A., Cavallo, A., 2014. The effect of Alpine metamorphism on an oceanic Cu-Fe sulfide ore: the Herin deposit, Western Alps, Italy. *Period. Mineral.* 83, 345–365.
- Filzmoser, P., Hron, K., Reimann, C., 2009. Principal component analysis for compositional data with outliers. *Environmetrics* 20, 621–632.
- Filzmoser, P., Hron, K., 2011. Robust statistical analysis. In: Pawlowsky-Glahn, V., Buccianti, A. (Eds.), *Compositional Data Analysis. Theory and Applications*. John Wiley & Sons, Chichester (UK), pp. 59–72.
- Fontana, E., Panseri, M., Tartarotti, P., 2008. Oceanic relict textures in the Mount Avic serpentinites, Western Alps. *Ofioliti* 33, 105–118.
- Fontana, E., Tartarotti, P., Panseri, M., Buscemi, S., 2015. Geological map of the Mount Avic massif (Western Alps Ophiolites). *J. Maps* 11, 126–135.
- Fouquet, Y., Cambon, P., Etoubeau, J., Charlou, J.L., Ondréas, H., Barriga, F.J.A.S., Cherkashov, G., Semkova, T., Poroshina, I., Bohn, M., Donval, J.P., Henry, K., Murphy, P., Rouxel, O., 2010. Geodiversity of hydrothermal processes along the Mid-Atlantic Ridge and ultramafic-hosted mineralization: a new type of oceanic Cu-Zn-Co-Au volcanogenic massive sulfide deposit. In: Rona, P.A., Devey, C.W., Dymont, J., Murton, B.J. (Eds.), *Diversity of Hydrothermal Systems on Slow Spreading Ocean Ridges*. American Geophysical Union, Washington, DC, pp. 321–367.
- Foustoukos, D.I., Seyfried, W.E., 2007. Fluid phase separation processes in submarine hydrothermal systems. *Rev. Mineral. Geochem.* 65, 213–239.
- Frost, B.R., Beard, J.S., 2007. On silica activity and serpentinization. *J. Petrol.* 48, 1351–1368.
- Fujii, M., Okino, K., Sato, T., Sato, H., Nakamura, K., 2016. Origin of magnetic highs at ultramafic hosted hydrothermal systems: insights from the Yokoniwa site of Central Indian Ridge. *Earth Planet. Sci. Lett.* 441, 26–37.
- Gahlan, H.A., Arai, S., Ahmed, A.H., Ishida, Y., Abdel-Aziz, Y.M., Rahimi, A., 2006. Origin of magnetite veins in serpentinite from the Late Proterozoic Bou-Azzer ophiolite, Anti-Atlas, Morocco: An implication for mobility of iron during serpentinization. *J. Afr. Earth Sci.* 46, 318–330.
- Giacometti, F., Evans, K.A., Rebay, G., Cliff, J., Tomkins, A.G., Rossetti, P., Vaggelli, G., Adams, D.T., 2014. Sulfur isotope evolution in sulfide ores from Western Alps: assessing the influence of subduction-related metamorphism. *Geochem. Geophys. Geosyst.* 15, 3808–3829.
- Govindaraju, K., 1994. Compilation of working values and sample description for 383 geostandards. *Geostandard Newslett.* 18, 1–158.
- Groppe, C., Rinaudo, C., Cairo, S., Gastaldi, D., Compagnoni, R., 2006. Micro-Raman spectroscopy for a quick and reliable identification of serpentine minerals from ultramafics. *Eur. J. Mineral.* 18, 319–329.
- Hekinian, R., Hoffer, M., Larque, P., Cheminee, J.L., Stoffers, P., Bideau, D., 1993. Hydrothermal Fe and Si oxyhydroxide deposits from South Pacific intraplate volcanoes and East Pacific Rise axial and off-axial regions. *Econ. Geol.* 88, 2099–2121.
- Hiess, J., Condon, D.J., McLean, N., Noble, S.R., 2012. 238U/235U systematics in terrestrial uranium-bearing minerals. *Science* 335, 1610–1614.
- Ho, P.C., Palmer, D.A., Mesmer, R.E., 1994. Electrical of aqueous sodium chloride solutions to 600 C and 300 MPa. *J. Solution Chem.* 23, 997–1018.
- Ho, P.C., Bianchi, H., Palmer, D.A., Wood, R.H., 2000. Conductivity of dilute aqueous electrolyte solutions at high temperatures and pressures using a flow cell. *J. Solution Chem.* 29, 217–235.
- Ho, P.C., Palmer, D.A., Gruskiewicz, M.S., 2001. Conductivity measurements of dilute aqueous HCl solutions to high temperatures and pressures using a flow-through cell. *J. Phys. Chem. B* 105, 1260–1266.
- Jaffey, A.H., Flynn, K.F., Glendenin, L.E., Bentley, W.T., Essling, A.M., 1971. Precision measurement of half-lives and specific activities of ²³⁵U and ²³⁸U. *Phys. Rev. C* 4, 1889.
- Janecky, D.R., Seyfried, W.E., 1984. Formation of massive sulfide deposits on oceanic ridge crests: Incremental reaction models for mixing between hydrothermal solutions and seawater. *Geochim. Cosmochim. Acta* 48, 2723–2738.
- Jupp, T.E., Schultz, A., 2004. Physical balances in seafloor hydrothermal convection cells. *J. Geophys. Res.-Sol. Earth* 109 (B5).
- Klein, F., Bach, W., Jöns, N., McCollom, T., Moskowitz, B., Berquó, T., 2009. Iron partitioning and hydrogen generation during serpentinization of abyssal peridotites from 15 N on the Mid-Atlantic Ridge. *Geochim. Cosmochim. Acta* 73, 6868–6893.
- Le Roux, L.J., Glendenin, L.E., 1963. Half-life of ²³²Th. In: *Proceedings of the National Meeting on Nuclear Energy: Application of Isotopes and Radiation*, Pretoria, pp. 83–94.
- Lombardo, B., Rubatto, D., Castelli, D., 2002. Ion microprobe U-Pb dating of zircon from a Monviso metaplagiogranite: implications for the evolution of the Piedmont-Liguria Tethys in the Western Alps. *Ofioliti* 27, 109–117.
- Ludwig, K.R., 2012. *User's Manual for ISOPLOT 3.75*, A Geochronological Toolkit for Microsoft Excel. Berkeley Geochronology Center. Spec. Pub. 5.
- Manatschal, G., Müntener, O., 2009. A type sequence across an ancient magma-poor ocean-continent transition: the example of the western Alpine Tethys ophiolites. *Tectonophysics* 473, 4–19.
- Manatschal, G., Sauter, D., Karpoff, A.M., Masini, E., Mohn, G., Lagabrielle, Y., 2011. The Chenailler Ophiolite in the French/Italian Alps: an ancient analogue for an oceanic core complex? *Lithos* 124, 169–184.
- Marques, A.F.A., 2005. *Geology and Genesis of Sulfide Mineralization in the Rainbow Ultramafic-Hosted Seafloor Hydrothermal System*. Dissertation. University of Lisbon.
- Marques, A.F.A., Barriga, F.J., Chavagnac, V., Fouquet, Y., 2006. Mineralogy, geochemistry, and Nd isotope composition of the Rainbow hydrothermal field, Mid-Atlantic Ridge. *Miner. Deposita* 41, 52–67.
- Marques, A.F.A., Barriga, F.J., Scott, S.D., 2007. Sulfide mineralization in an ultramafic-rock hosted seafloor hydrothermal system: From serpentinization to the formation of Cu-Zn-(Co)-rich massive sulfides. *Mar. Geol.* 245, 20–39.
- Martin, S., Rebay, G., Kienast, J., Mével, C., 2008. An eclogitized oceanic palaeo-hydrothermal field from the St. Marcel Valley (Italian Western Alps). *Ofioliti* 33, 49–63.
- McCaig, A.M., Cliff, R.A., Escartin, J., Fallick, A.E., MacLeod, C.J., 2007. Oceanic detachment faults focus very large volumes of black smoker fluids. *Geology* 35, 935–938.

- Melekestseva, I.Y., Zaykov, V.V., Nimis, P., Tret'yakov, G.A., Tessalina, S.G., 2013. Cu–(Ni–Co–Au)-bearing massive sulfide deposits associated with mafic–ultramafic rocks of the Main Urals Fault, South Urals: Geological structures, ore textural and mineralogical features, comparison with modern analogs. *Ore Geol. Rev.* 52, 18–36.
- Melekestseva, I.Y., Tret'yakov, G.A., Nimis, P., Yuminov, A.M., Maslennikov, V.V., Maslennikova, S.P., Kotlyarov, V.A., Beltenev, V.E., Danyushevsky, L.V., Large, R., 2014. Barite-rich massive sulfides from the Semenov-1 hydrothermal field (Mid-Atlantic Ridge, 13°30.87'N): Evidence for phase separation and magmatic input. *Mar. Geol.* 349, 37–54.
- Mellini, M., Rumori, C., Viti, C., 2005. Hydrothermally reset magmatic spinels in retrograde serpentinites: formation of “ferritchromit” rims and chlorite aureoles. *Contrib. Mineral. Petrol.* 149, 266–275.
- Merlini, A., Grieco, G., Diella, V., 2009. Ferritchromite and chromian-chlorite formation in mélange-hosted Kalkan chromitite (Southern Urals, Russia). *Am. Mineral.* 94, 1459–1467.
- Mével, C., 2003. Serpentinization of abyssal peridotites at mid-ocean ridges. *C. R. Geosci.* 335, 825–852.
- Montel, J.M., Foret, S., Veschambre, M., Nicollet, C., Provost, A., 1996. Electron microprobe dating of monazite. *Chem. Geol.* 131, 37–53.
- Nadoll, P., Koenig, A.E., 2011. LA-ICP-MS of magnetite: methods and reference materials. *J. Anal. Atom. Spectrom.* 26, 1872–1877.
- Nadoll, P., Angerer, T., Mauk, J.L., French, D., Walshe, J., 2014. The chemistry of hydrothermal magnetite: a review. *Ore Geol. Rev.* 61, 1–32.
- Nadoll, P., Mauk, J.L., Leveille, R.A., Koenig, A.E., 2015. Geochemistry of magnetite from porphyry Cu and skarn deposits in the southwestern United States. *Miner. Deposita* 50, 493–515.
- Niu, Y., 2004. Bulk-rock major and trace element compositions of abyssal peridotites: implications for mantle melting, melt extraction and post-melting processes beneath mid-ocean ridges. *J. Petrol.* 45, 2423–2458.
- O'Neill, H.S.C., Palme, H., 1998. Composition of the silicate Earth: implications for accretion and core formation. In: Jackson, I. (Ed.), *The Earth's Mantle: Composition, Structure and Evolution*. Cambridge University Press, pp. 3–126.
- Panseri, M., Fontana, E., Tartarotti, P., 2008. Evolution of rodingitic dykes: metasomatism and metamorphism in the Mount Avic serpentinites (Alpine Ophiolites, southern Aosta Valley). *Ophioliti* 33, 165–185.
- Paraskevopoulos, G.M., Economou, M., 1980. Genesis of magnetite ore occurrences by metasomatism of chromite ores in Greece. *Neues. Jb. Miner. Abh.* 140, 29–53.
- Paulick, H., Bach, W., Godard, M., De Hoog, J.C.M., Suhr, G., Harvey, J., 2006. Geochemistry of abyssal peridotites (Mid-Atlantic Ridge, 15°20' N, ODP Leg 209): implications for fluid/rock interaction in slow spreading environments. *Chem. Geol.* 234, 179–210.
- Pester, N.J., Ding, K., Seyfried, W.E., 2014. Magmatic eruptions and iron volatility in deep-sea hydrothermal fluids. *Geology* 42, 255–258.
- Piccardo, G.-B., 2008. The Jurassic Ligurian Tethys, a fossil ultraslow-spreading ocean: the mantle perspective. In: Grégoire, M., Coltorti, M. (Eds.), *Metamorphism in oceanic and continental lithospheric mantle*, vol. 293. Geological Society, London, pp. 11–33. Special Publication.
- Polino, R., Martin, S., Malusà, M., Mosca, P., Bonetto, F., Baggio, P., Baster, I., Bertolo, D., Carraro, F., Fontan, D., Gianotti, F., Monopoli, B., Perello, P., Schiavo, A., Venturini, G., Vuillermoz, R., 2014. Note illustrative della carta geologica d'Italia alla scala 1:50.000 Aosta F. 90. *Ispra-Servizio Geologico d'Italia*.
- Puteanus, D., Glasby, G.P., Stoffers, P., Kundendorf, H., 1991. Hydrothermal iron-rich deposits from the Teahitia-Mehitia and Macdonald hot spot areas, Southwest Pacific. *Mar. Geol.* 98, 389–409.
- Renna, M.R., Tribuzio, R., 2011. Olivine-rich troctolites from Ligurian ophiolites (Italy): evidence for impregnation of replacive mantle conduits by MORB-type melts. *J. Petrol.* 52, 1763–1790.
- Rona, P.A., 1988. Hydrothermal mineralization at oceanic ridges. *Can. Mineral.* 26, 431–465.
- Rossetti, P., Gatta, G.D., Diella, V., Carbonin, S., Della Giusta, A., Ferrario, A., 2009. The magnetite ore districts of the southern Aosta Valley (Western Alps, Italy): a mineralogical study of metasomatized chromite ore. *Mineral. Mag.* 73, 737–751.
- Routhier, P., 1963. *Les Gisements Métallifères: Géologie Et Principes De Recherche*. Masson, Paris.
- Sanfiliippo, A., Tribuzio, R., Tiepolo, M., 2014. Mantle–crust interactions in the oceanic lithosphere: constraints from minor and trace elements in olivine. *Geochim. Cosmochim. Acta* 141, 423–439.
- Sawyer, G.M., Oppenheimer, C., Tsanev, V.I., Yirgu, G., 2008. Magmatic degassing at Erta'Ale volcano, Ethiopia. *J. Volcanol. Geoth. Res.* 178, 837–846.
- Schmid, S.M., Fügenschuh, B., Kissling, E., Schuster, R., 2004. Tectonic map and overall architecture of the Alpine orogen. *Ecolage Geol. Helv.* 97, 93–117.
- Schwartz, S., Guillot, S., Reynard, B., Lafay, R., Debret, B., Nicollet, C., Lanari, P., Auzende, A.L., 2013. Pressure–temperature estimates of the lizardite/antigorite transition in high pressure serpentinites. *Lithos* 178, 197–210.
- Seyfried Jr, W.E., 1987. Experimental and theoretical constraints on hydrothermal alteration processes at mid-ocean ridges. *Annu. Rev. Earth Planet. Sci.* 15, 317.
- Seyfried, W.E., Foustoukos, D.I., Allen, D.E., 2004. Ultramafic-hosted hydrothermal systems at mid-ocean ridges: chemical and physical controls on pH, redox and carbon reduction reactions. In: German, C.R., Lin, J., Parson, L.M. (Eds.), *Mid-Ocean Ridges: Hydrothermal Interactions Between the Lithosphere and Oceans*. American Geophysical Union, Washington, DC, pp. 267–284.
- Seyfried, W.E., Pester, N., Fu, Q., 2010. Phase equilibria controls on the chemistry of vent fluids from hydrothermal systems on slow spreading ridges: reactivity of plagioclase and olivine solid solutions and the pH–silica connection. In: Rona, P.A., Devey, C.W., Dymont, J., Murton, B.J. (Eds.), *Diversity of Hydrothermal Systems on Slow Spreading Ocean Ridges*. American Geophysical Union, Washington, DC, pp. 297–320.
- Seyfried, W.E., Pester, N.J., Ding, K., Rough, M., 2011. Vent fluid chemistry of the Rainbow hydrothermal system (36°N, MAR): phase equilibria and in situ pH controls on seafloor alteration processes. *Geochim. Cosmochim. Acta* 75, 1574–1593.
- Singh, S.C., Crawford, W.C., Carton, H., Seher, T., Combiér, V., Cannat, M., Canales, J.P., Düsünür, D., Escartin, J., Miranda, J.M., 2006. Discovery of a magma chamber and faults beneath a Mid-Atlantic Ridge hydrothermal field. *Nature* 442, 1029–1032.
- Suhr, G., Hellebrand, E., Johnson, K., Brunelli, D., 2008. Stacked gabbro units and intervening mantle: a detailed look at a section of IODP Leg 305, Hole U1309D. *Geochem. Geophys. Geosyst.* 9.
- Szitar, F., Dymont, J., Fouquet, Y., Honsho, C., Horen, H., 2014. The magnetic signature of ultramafic-hosted hydrothermal sites. *Geology* 42, 715–718.
- Stampfli, G.M., 2000. Tethyan oceans. *Geol. Soc. Lond. Spec. Publ.* 173, 1–23. Spec. Publ.
- Stella, A., 1916. *Le miniere di Cogne (Val d'Aosta)*. S.A.I.G.A. Barabino, Genova.
- Stella, A., 1921. *Le miniere di ferro d'Italia*. Lattes, Torino.
- Tartarotti, P., Festa, A., Benciolini, L., Balestro, G., 2015. Mantle-cover sequence in the Western Alps metaophiolites: a key to recognize remnants of an exhumed Oceanic Core Complex (OCC). *Rend. Online Soc. Geol. It.* 35 (Suppl. 2).
- Templ, M., Hron, K., Filzmoser, P., 2011. robCompositions: an R-package for robust statistical analysis of compositional data. In: Pawlowsky-Glahn, V., Buccianti, A. (Eds.), *Compositional Data Analysis. Theory and Applications*. John Wiley & Sons, Chichester (UK), pp. 341–355.
- Tivey, M.A., Dymont, J., 2010. The magnetic signature of hydrothermal systems in slow spreading environments. In: Rona, P.A., Devey, C.W., Dymont, J., Murton, B.J. (Eds.), *Diversity of Hydrothermal Systems on Slow Spreading Ocean Ridges*. American Geophysical Union, Washington, DC, pp. 43–66.
- Tumiati, S., Martin, S., Godard, G., 2010. Hydrothermal origin of manganese in the high-pressure ophiolite metasediments of Praborna ore deposit (Aosta Valley, Western Alps). *Eur. J. Mineral.* 22, 577–594.
- Tumiati, S., Godard, G., Martin, S., Malaspina, N., Poli, S., 2015. Ultra-oxidized rocks in subduction mélanges? Decoupling between oxygen fugacity and oxygen availability in a Mn-rich metasomatic environment. *Lithos* 226, 116–130.
- Von Damm, K.L., 2004. Evolution of the hydrothermal system at East Pacific Rise 9°50'N: geochemical evidence for changes in the upper oceanic crust. In: German, C.R., Lin, J., Parson, L.M. (Eds.), *Mid-Ocean Ridges: Hydrothermal Interactions Between the Lithosphere and Oceans*. American Geophysical Union, Washington, DC, pp. 285–304.
- Whitney, D.L., Evans, B.W., 2010. Abbreviations for names of rock-forming minerals. *Am. Mineral.* 95, 185–187.
- Wolery, T.J., Jarek, R.L., 2003. *Software User's Manual EQ3/6 (Version 8.0)*. Sandia National Laboratories, Albuquerque, New Mexico.
- Wolery, T.J., 2013. EQ3/6 – Software for Geochemical Modeling, Version 8.0a. Lawrence Livermore National Laboratory, Livermore, California.
- Yıldırım, N., Dönmez, C., Kang, J., Lee, I., Pirajno, F., Yıldırım, E., Günay, K., Seo, J.H., Farquhar, J., Chang, S.W., 2016. A magnetite-rich Cyprus-type VMS deposit in Ortaklar: a unique VMS style in the Tethyan metallogenic belt, Gaziantep, Turkey. *Ore Geol. Rev.* 79, 425–442.